TKK Dissertations 113
Espoo 2008

FABRICATION OF InGaN QUANTUM WELLS FOR LED APPLICATIONS

Doctoral Dissertation

Sami Suihkonen

Helsinki University of Technology
Faculty of Electronics, Communications and Automation
Department of Micro and Nanosciences

TKK Dissertations 113
Espoo 2008

FABRICATION OF InGaN QUANTUM WELLS FOR LED APPLICATIONS

Doctoral Dissertation

Sami Suihkonen

Dissertation for the degree of Doctor of Science in Technology to be presented with due permission of the Faculty of Electronics, Communications and Automation for public examination and debate in Auditorium As1 at Helsinki University of Technology (Espoo, Finland) on the 11th of April, 2008, at 12 noon.

Helsinki University of Technology
Faculty of Electronics, Communications and Automation
Department of Micro and Nanosciences

Teknillinen korkeakoulu
Elektroniikan, tietoliikenteen ja automaation tiedekunta
Mikro- ja nanotekniikan laitos

Distribution:
Helsinki University of Technology
Faculty of Electronics, Communications and Automation
Department of Micro and Nanosciences
P.O. Box 3500
FI - 02015 TKK
FINLAND
Tel. +358-9-4511
Fax +358-9-451 3128
E-mail: sami.suihkonen@tkk.fi

ISBN 978-951-22-9286-8
ISBN 978-951-22-9287-5 (PDF)
ISSN 1795-2239
ISSN 1795-4584 (PDF)
URL: http://lib.tkk.fi/Diss/2008/isbn9789512292875/

TKK-DISS-2450

Multiprint Oy
Espoo 2008

ABSTRACT OF DOCTORAL DISSERTATION	HELSINKI UNIVERSITY OF TECHNOLOGY P. O. BOX 1000, FI-02015 TKK http://www.tkk.fi

Author Sami Suihkonen

Name of the dissertation

Fabrication of InGaN quantum wells for LED applications

Manuscript submitted 14.01.2008	Manuscript revised 28.02.2008
Date of the defence 11.04.2008	
☐ Monograph	☒ Article dissertation (summary + original articles)

Faculty	Faculty of Electronics, Communications and Automation
Department	Department of Micro and Nanosciences
Field of research	Optoelectronics
Opponent(s)	Prof. Michael Kneissl
Supervisor	Docent Markku Sopanen
Instructor	-

Abstract

In this thesis fabrication and properties of InGaN quantum wells (QWs) for light emitting diode (LED) applications is studied. Metal-organic vapor phase epitaxy (MOVPE) is used to grow InGaN/(InAl)GaN multiple quantum well (MQW) and LED structures on GaN/sapphire substrates. Also a multistep growth method for the growth of GaN on sapphire is investigated. The method enables a tenfold reduction of threading dislocation (TD) density in the GaN layer compared to conventional growth methods. The objective of this work is to study the physics of InGaN QWs and to improve the performance of InGaN MQW structures used in near-UV, blue and green LEDs. The quality of quantum wells is analyzed by x-ray diffraction (XRD), atomic force microscopy (AFM), and photoluminescence (PL) measurements. The LED structures are characterized also by electroluminescence (EL) measurements.

Various MOVPE growth parameters of InGaN/GaN QWs are evaluated for growth of MQW structures emitting blue light. Smooth surface morphology of the MQW stack is achieved by introducing a small amount of H_2 during the MOVPE growth of the GaN barrier layers. The effect of TD density on the performance of near-UV, blue, and green LEDs is studied by fabricating LED structures on GaN buffers grown by the multistep method. Improved EL output power at high operating current density is observed in the blue LEDs fabricated on the multistep GaN buffers.

MOVPE growth of quaternary InAlGaN layers is investigated and InGaN/InAlGaN MQW structures for near-UV emission are presented. The internal quantum efficiency (IQE) of InGaN/InAlGaN MQW structures is found to be sensitive to the InAlGaN barrier layer composition and the strain state of the structure. A MQW structure emitting at 383 nm with an IQE of 45 % is presented.

Finally the origin of the high efficiency of InGaN QWs is discussed. The high efficiency is due to self-screening mechanism of TDs in In containing QWs. The height of the potential barrier formed around the TD depends on the In content of the QWs, and thus the effect of TDs on the performance of blue and green LEDs is different.

Keywords	Light emitting diodes, MOVPE, III-N materials, quantum wells
ISBN (printed) 978-951-22-9286-8	ISSN (printed) 1795-2239
ISBN (pdf) 978-951-22-9287-5	ISSN (pdf) 1795-4584
Language english	Number of pages 74+48
Publisher	TKK, Department of Micro and Nanosciences
Print distribution	TKK, Department of Micro and Nanosciences

☒ The dissertation can be read at http://lib.tkk.fi/Diss/2008/isbn9789512292875/

VÄITÖSKIRJAN TIIVISTELMÄ	TEKNILLINEN KORKEAKOULU PL 1000, 02015 TKK http://www.tkk.fi

Tekijä Sami Suihkonen

Väitöskirjan nimi

Fabrication of InGaN quantum wells for LED applications

Käsikirjoituksen päivämäärä 14.01.2008	Korjatun käsikirjoituksen päivämäärä 28.02.2008
Väitöstilaisuuden ajankohta 11.04.2008	
☐ Monografia	☒ Yhdistelmäväitöskirja (yhteenveto + erillisartikkelit)

Tiedekunta	Elektroniikan, tietoliikenteen ja automaation tiedekunta
Laitos	Mikro- ja nanotekniikan laitos
Tutkimusala	Optoelektroniikka
Vastaväittäjä(t)	Prof. Michael Kneissl
Työn valvoja	Dosentti Markku Sopanen
Työn ohjaaja	-

Tiivistelmä

Väitöskirjassa tutkittiin InGaN-kvanttikaivojen valmistusta ja ominaisuuksia. Erityisesti keskityttiin kvanttikaivojen käyttöön valoa emittoivissa diodeissa (LED). Kvanttikaivo- ja LED-rakenteet valmistettiin metallo-orgaanisella kaasufaasiepitaksialla (MOVPE) GaN/safiiri-alustakiteiden päälle. Työssä esitettiin myös monivaiheinen menetelmä GaN-ohutkalvojen valmistamiseksi. Monivaiheisella menetelmällä GaN kerroksessa etenevien dislokaatioiden määrää pystyttiin pienentämään kymmenesosaan verrattuna tavanomaisiin valmistusmenetelmiin. Väitöskirjatyön tavoitteena oli tutkia InGaN-kvanttikaivojen fysiikkaa ja parantaa InGaN-kvanttikaivojen ominaisuuksia UV-, sinisissä ja vihreissä LED-rakenteissa. Kvanttikaivojen laatua tutkittiin röntgendiffraktiolla, atomivoimamikroskopialla ja fotoluminesenssimittauksilla. LED-rakenteita tutkittiin myös elektroluminesenssimittauksilla.

Tässä työssä tutkittiin useiden eri MOVPE-valmistusprosessien vaikutusta sinisissä LED-rakenteissa käytettävien InGaN/GaN-kvanttikaivorakenteiden laatuun. Tasainen pinnan morfologia saavutettiin käyttämällä vetyä GaN-vallien valmistuksen aikana. Etenevien dislokaatioden vaikutusta UV-, sinisten ja vihreiden LED-rakenteiden ominaisuuksiin tutkittiin valmistamalla LED-rakenteet monivaiheisella menetelmällä valmistettujen GaN-kerrosten päälle. Tämä lisäsi sinisten LED-rakenteiden elektroluminesenssia, kun käytettiin suurta virrantiheyttä.

Myös InAlGaN-neliyhdisteiden MOVPE valmistusta tutkittiin ja UV-alueella emittoivia InGaN/InAlGaN-kvanttikaivorakenteita valmistettiin. InGaN/InAlGaN-kvanttikaivorakenteiden sisäisen kvanttihyötysuhteen havaittiin riippuvan InAlGaN-vallien kompositiosta ja kvanttikaivorakenteen jännityksestä. Tässä työssä esiteltiin myös 383 nm:n aallonpituudella ja 45 % kvanttihyötysuhteella emittoiva InGaN/InAlGaN kvanttikaivorakenne.

Lopuksi käsiteltiin InGaN kvanttikaivojen korkean hyötysuhteen syitä. Korkean hyötysuhteen havaittiin aiheutuvan dislokaatioiden itsesuojaavasta luonteesta InGaN kvanttikaivoissa. Dislokaatioden ympärille muodostuvan potentiaalivallin korkeus havaittiin riippuvan kaivojen In-pitoisuudesta, joten dislokaatioiden vaikutus sinisten ja vihreiden LED-rakenteiden ominaisuuksiin oli erilainen.

Asiasanat	LED, MOVPE, III-N materiaalit, kvanttikaivo
ISBN (painettu) 978-951-22-9286-8	ISSN (painettu) 1795-2239
ISBN (pdf) 978-951-22-9287-5	ISSN (pdf) 1795-4584
Kieli englanti	Sivumäärä 74+48
Julkaisija	TKK, Mikro- ja nanotekniikan laitos
Painetun väitöskirjan jakelu	TKK, Mikro- ja nanotekniikan laitos
☒ Luettavissa verkossa osoitteessa http://lib.tkk.fi/Diss/2008/isbn9789512292875/	

Preface

The work done for this thesis has been carried out in the Department of Micro and Nanosciences at Helsinki University of Technology (TKK) during 2005-2008.

First I want to express my gratitude to Docent Markku Sopanen, the supervisor of this thesis, for the guidance throughout this work and for the interesting research topic. I want to thank also Professor Harri Lipsanen for the possibility to work at the Department of Micro and Nanosciences. I am grateful to Dr. Maxim Odnoblyudov and Dr. Vladislav Bougrov from OptoGaN Oy and Abraham-Ioffe Institute, for their support and our fruitful collaboration regarding my research. I want also to thank the people of the Optoelectronics and Nanotechnology groups, especially all the people who are working or have worked in the GaN research team, Mr. Olli Svensk, Mr. Pekka Törmä, Mr. Muhammad Ali, and Dr. Teemu Lang. It has been a real pleasure to work and even greater pleasure to slack off with you guys. Also many thanks to Dr. Marco Mattila for invaluable support concerning everything between MOVPE technology and LaTeX formatting.

I also want to thank my girlfriend Riikka for love and support and for understanding the odd working hours needed to finish this thesis. Also big thanks to my parents for supplying me enough LEGO blocks for my experiments during the early years of my research work.

This work has been partly funded by the National Graduate School in Material Physics, the Vaisala Fund and OptoGaN Oy.

Espoo, 12.01.2008

Sami Suihkonen

Contents

List of publications

This thesis consists of an overview and of the following publications which are referred to in the text by their Roman numerals.

I S. Suihkonen, J. Sormunen, V. T. Rangel-Kuoppa, H. Koskenvaara and M. Sopanen, *Growth of InN by vertical flow MOVPE*, Journal of Crystal Growth **291**, 8 (2006).

II S. Suihkonen, T. Lang, O. Svensk, J. Sormunen, P. T. Törmä, M. Sopanen, H. Lipsanen, M. A. Odnoblyudov and V. E. Bougrov, *Control of the morphology of InGaN/GaN quantum wells grown by metalorganic chemical vapor deposition*, Journal of Crystal Growth **300**, 324 (2007).

III S. Suihkonen, O. Svensk, T. Lang, H. Lipsanen, M. A. Odnoblyudov and V. E. Bougrov, *The effect of InGaN/GaN MQW hydrogen treatment and threading dislocation optimization on GaN LED efficiency*, Journal of Crystal Growth **298**, 740 (2007).

IV S. Suihkonen, O. Svensk, P.T. Törmä, M. Ali, M. Sopanen, H. Lipsanen, M. A. Odnoblyudov and V. E. Bougrov, *MOVPE growth and characterization of InAlGaN films and InGaN/InAlGaN MQW structures*, Journal of Crystal Growth, IN PRESS.

V T. Lang, M. A. Odnoblyudov, V. E. Bougrov, A. E. Romanov, S. Suihkonen, M. Sopanen and H. Lipsanen, *Multistep method for threading dislocation density reduction in MOCVD grown GaN epilayers*, physica status solidi (a) **203**, No. 10, R76 (2006).

VI T. Lang, M. Odnoblyudov, V. Bougrov, S. Suihkonen, M. Sopanen and H. Lipsanen, *Morphology optimization of MOCVD-grown GaN nucleation layers by the multistep technique*, Journal of Crystal Growth **292**, 26 (2006).

VII M. Ali, S. Suihkonen, O. Svensk, P. T. Törmä, M. Sopanen, H. Lipsanen, M. A. Odnoblyudov and V. E Bougrov, *Study of Composition Control and Capping of MOVPE Grown InGaN/$In_xAl_yGa_{1-x-y}N$ MQW Structures*, physica status solidi (c), ACCEPTED FOR PUBLICATION.

Author's contribution

The author has written the manuscripts and designed the experiments for publications I, II, III and IV.

The author has performed the major part of the sample fabrication, data collection and data analysis for publications I, II, III and IV.

The author has contributed to the design of experiments, performed parts of the sample fabrication, and data analysis and assisted in writing of the manuscript for publication VII.

The author has contributed to the design of experiments and performed parts of the sample fabrication for publications V and VI.

1 Introduction

In the recent years the development in the field of III-N semiconductor technology has been spectacular. Numerous GaN-based devices including light emitting diodes (LEDs), laser diodes (LDs), photo detectors and high power microwave power switches have been developed and brought to the market. GaN-based laser diodes enable more efficient data storage in the high density DVD standards, and LEDs are used in various lighting applications including flashlights, automotive lighting, traffic signals and indoor lighting. The future especially for general lighting applications is promising, since white light can be produced by exciting wide band phosphors by blue or UV-LEDs [1, 2].

The driving force behind the fast development of III-N semiconductors has been the demand for short wavelength emitters. To date there exists only a few semiconductor material systems suitable for such applications. Several II-VI semiconductors such as ZnSe and ZnS have been extensively studied but the short lifetime of devices limits their use [1]. Of the II-VI materials zinc oxide (ZnO) holds promises as a material for blue and UV optoelectronics, but difficulties in p-type doping hinder the use of ZnO in devices [3]. Therefore, the III-N material system is currently the only practical solution for short wavelength semiconductor emitters. Several technical innovations during the '90s enabled the fast progress in the development of blue and UV LEDs and LDs. Among the key inventions is the use of a low temperature AlN nucleation layer. The technique was developed in 1986 by Akasaki *et al.* [4]. By utilizing the nucleation layer the dislocation density of GaN grown on sapphire was reduced significantly. In 1991 sufficient p-type conductivity for LED and LD operation was obtained by thermal annealing of Mg-doped GaN by Nakamura *et al.* [5]. The first nitride-based LED with external quantum efficiency of 2.7 % was commercialized in 1993 [6]. The first LEDs employing InGaN/GaN quantum wells were fabricated in 1995 [7]. Currently the III-nitrides are considered as the best material system for efficient solid-state lighting. One of the next challenges is to realize efficient InAlGaN based UV-emitting devices. UV semiconductor light sources are required for a number of applications including general lighting, sterilization, decontamination and for next generation high density optical storage [8, 9].

Although III-N materials have been under extensive study there still exists several problems related to the operation of high power GaN-based light emitting devices. One is the large dislocation density of GaN and AlGaN buffers that reduces device

performance at high current densities. The typical dislocation density in GaN LED structures is six orders of magnitude higher than in conventional AlGaAs or AlInGaP LED structures. Despite the high dislocation density, which would forbid the operation of LEDs made of conventional III-V semiconductors, GaN-based LEDs function with surprisingly good efficiency. The reason behind the good performance of GaN light emitting devices is still not clear. A defect insensitive emission mechanism in In containing (Al,In,Ga)N alloys has been proposed [10]. Also a defect screening mechanism in InGaN quantum wells has been suggested [11]. Nevertheless, fabrication of high quality quantum well structures, especially for emission in the UV range is a challenging task. Some of these problems are addressed in this thesis, and methods are presented for fabrication of efficient green, blue, and near-UV emitting structures.

Chapter two of this thesis describes the fundamental properties of III-N semiconductors that are needed to understand the basic operation of GaN-based LEDs. The experimental methods for sample fabrication and characterization used in this work are presented in chapter three. Chapter four describes epitaxial growth of III-N semiconductors in further detail. Chapter five presents a typical GaN-LED structure and its properties. In chapter six fabrication of InGaN/(InAl)GaN quantum wells and their properties are discussed in detail and the experimental results of this thesis are presented.

2 Fundamentals of III-N semiconductors

This chapter provides an introduction to the crystalline structure and electronic properties of III-nitride semiconductor materials and to the use of these materials in optoelectronic applications. Basic knowledge of these properties is crucial for understanding the fundamentals of quantum well based light emitting sources.

2.1 Crystal structure

In semiconductor materials atoms are organized in a three dimensional lattice, where the same periodic structure is repeated over the space of the crystal. The group III-nitrides can crystallize either in hexagonal wurtzite or zinc blende structures. Both of these structures can be grown by epitaxial thin film methods and have been extensively studied. The wurtzite structure is thermodynamically more stable and is more used in optoelectronic applications. In this work only wurtzite structures are investigated so further description of the zinc blende structure is omitted.

The hexagonal wurtzite unit cell of GaN is sketched in Fig. 2.1, where the sub lattices of gallium and nitrogen atoms are shown in different colors. In hexagonal wurtzite lattice atoms are tetrahedrally bonded to the nearest neighbors, and the unit cell is described by the lattice parameters c, a and u. The lattice constant c defines the spacing of two identical hexagonal lattice planes, and the lattice parameter a describes the distance of atoms in the hexagonal lattice plane. The dimensionless parameter u characterizes the bond length along the c-axis, and provides information of the distortion of the unit cell. Along the c-axis a stacking sequence of hexagonal GaN bilayers can be found. This is marked in Fig. 2.1 by A and B. The other group III-N semiconductors, InN, AlN and their ternary and quaternary compounds have the same crystalline structure, in which group-III atoms occupy the sublattice shown with Ga atoms in Fig. 2.1. Lattice constants a, c and u for GaN, InN, AlN are given in Table 2.1 [1].

The presence of the bilayers A and B results in an internal asymmetry along the c-axis. This means that the direction of the atomic bonds are different along the [0001] and [000$\bar{1}$] directions. This results in an internal polarity of the film, and is defined by the direction of the group-III–N bond between the bilayers (along the

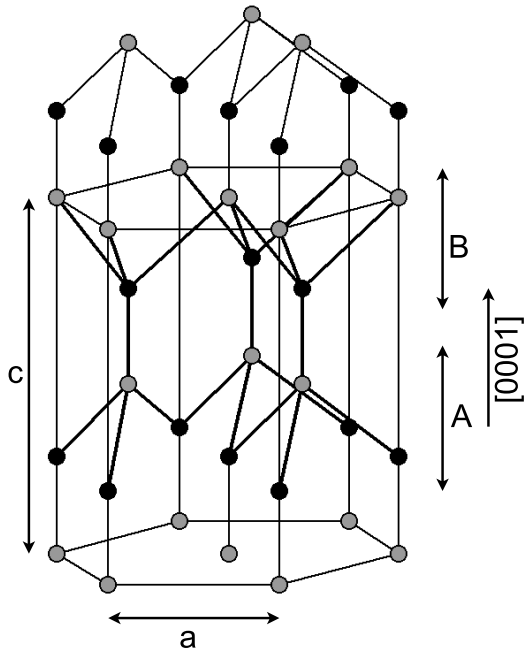

Figure 2.1. Hexagonal wurtzite crystal structure of GaN. The film is Ga-polar if black depicts N atoms, and N-polar if gray depicts N atoms and the surface of the film is located on top.

Table 2.1. Lattice constants a, c and u for GaN, InN and AlN.

Lattice constant	**GaN**	**InN**	**AlN**
a (Å)	3.189	3.534	3.111
c (Å)	5.185	5.718	4.978
u	0.377	0.382	0.379

c-axis) with respect to the surface normal of the film. If in this bond the nitrogen atoms are placed on top of the group-III atoms the film is called Ga- or [0001]-polar and if the group-III atoms are on top of N atoms the films is called N- or [000$\bar{1}$]-polar. This is sketched also in Fig. 2.1. The polarity of the films has a major effect on both the surface properties and on the piezoelectric field of the group-III nitrides. The effect of polarity has been widely investigated both theoretically and experimentally [12–14]. Surprisingly the polarity varies with different growth methods, GaN grown on (0001) sapphire by molecular beam epitaxy (MBE) is commonly N-polar, and metalorganic vapor phase epitaxy (MOVPE) grown Ga-polar [13, 14]. All the samples studied in this work were grown by MOVPE and were Ga-polar.

The deviation of the GaN unit cell from the ideal hexagonal wurtzite geometry and the strong ionic character of the III-N bond are the origins of polarization properties of wurtzite III-N semiconductors. The total polarization in the crystal in the

absence of external fields is the sum of spontaneous and piezoelectric polarizations. Spontaneous polarization is caused by the deviation of the unit cell from the ideal hexagonal structure. Due to the crystal symmetry the polarization is aligned along the [0001] direction, with the positive direction pointing parallel to the [0001]-axis. In Ga-polar GaN films the spontaneous field points towards the surface plane of the film [15].

The spontaneous polarization constants p_{sp} for binary III-N materials according to Ref. 15 are shown in Table 2.2.

Table 2.2. Spontaneous (p_{sp}) and piezoelectric constants (e_{31} and e_{33}) of group-III nitrides.

Parameter (C/m^2)	**GaN**	**InN**	**AlN**
p_{sp}	-0.029	-0.032	-0.081
e_{31}	-0.49	-0.57	-0.60
e_{33}	0.73	0.97	1.46

The piezoelectric polarization is caused by strain induced deformation of lattice parameters a, c and u. In hexagonal wurtzite lattice the piezoelectric polarization p_{pe} along the [0001]-axis depends on two independent piezoelectric coefficients e_{31} and e_{33} as

$$\delta p_{pe} = e_{33}\frac{c - c_0}{c_0} + 2e_{31}\frac{a - a_0}{a_0}, \tag{2.1}$$

where a_0 and c_0 are the equilibrium values of the lattice parameters [15]. Eq. 2.1 omits the polarization caused by shear strain, as it is not present in epitaxial structures. Starting from Eq. 2.1 it can be shown that in epitaxial III-N layers under tensile strain the polarization is always negative, and in layers under compressive strain the polarization is positive.

The electric field is connected to the polarization p by the relative dielectric constant $\epsilon_r(x)$ of the material according to

$$E = -\frac{p}{\epsilon_r(x)\epsilon_0}. \tag{2.2}$$

The effect of the built-in electric field in the heterojunctions of III-N semiconductors is described in more detail in section 2.3. A thorough description of spontaneous and piezoelectric polarization in III-V semiconductors can be found in Ref. 15.

2.2 Electronic band structure

In crystals the periodic arrangement of atoms modifies the single atom energy states into energy bands. These energy bands allow the movement of electrons in the crystal. In semiconductors there exists an energy band gap between energy bands. In this energy band configuration the higher energy band is called the conduction band, and the lower energy band the valence band. In direct band gap semiconductors the conduction band minimum (CBM) is located at the same electron wave vector (k) value as the valence band maximum (VBM). Direct band gap semiconductors are especially important for optoelectronic applications since radiative transitions from CBM to VBM have a much higher probability than in indirect band gap semiconductors.

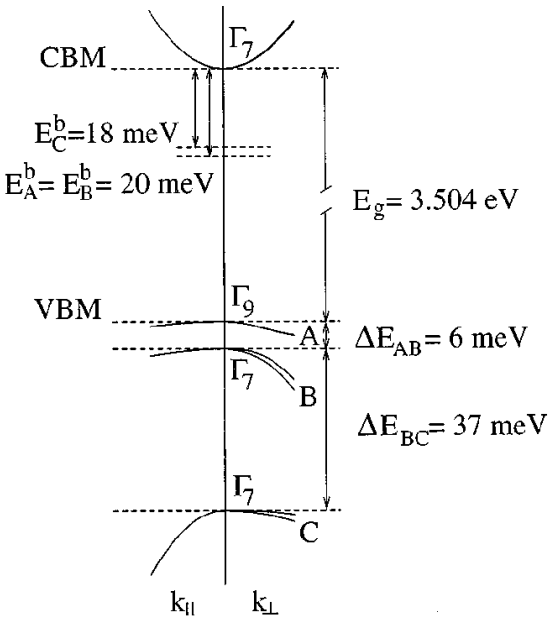

Figure 2.2. Calculated electronic band structure of hexagonal wurtzite GaN near the point $\vec{k}$=0 [16]. The directions parallel and perpendicular to the c-axis are denoted by $k_{||}$ and $k_{\perp}$, respectively.

Fig. 2.2 shows the calculated electronic band structure of hexagonal wurtzite GaN near the fundamental gap at $\vec{k}$=0 in the $\vec{k}$-space. The VBM and the CBM have the same $\vec{k}$-value, and the valence band is split into three different bands (A, B and C) by crystal field and spin orbit coupling. The bands and their corresponding exciton energies (E^b) are labeled in Fig. 2.2. The band gap value (E_g) shown in Fig. 2.2 is a calculated value at the temperature of 40 K. At room temperature the experimental band gap of GaN is 3.44 eV [17].

The major technological advantage of the III-N material system is that by alloying GaN with InN and AlN the band gap of the ternary or quaternary alloy can be

tuned in a controllable fashion. Fig. 2.3 shows the band gap versus the lattice parameter a of the III-N materials. In principle the band gap of III-N alloys can be varied continuously from 6.2 eV (pure AlN) to 0.7 eV (pure InN). Until recently the commonly quoted value for the optical band gap of InN was 1.89 eV, but new measurements have shown evidence of a much smaller band gap between 0.65 and 0.9 eV [18–20, and Publ. I]. The energy range from 6.2 eV to 0.7 eV covers the spectral range from deep UV to infrared. However, as the In or Al content of InGaN and AlGaN films is increased the growth of high quality material becomes more difficult due to the different optimum growth conditions of In and Al containing III-N alloys [21]. The difficulty of growth currently limits the possible wavelength range of GaN-based emitters from near UV to green. The growth of III-N materials will be discussed in more detail in chapter 4.

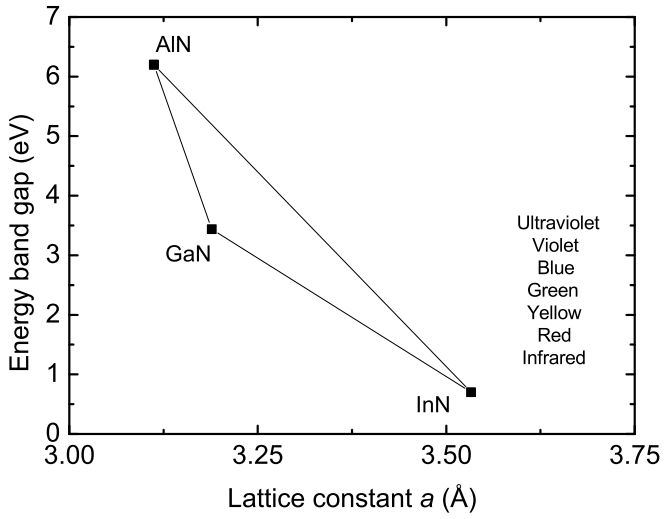

Figure 2.3. Band gap and lattice constant a of the most important III-N semiconductors.

In ternary and quaternary compounds the change of the band gap energy with composition can be described by linear interpolation with the inclusion of a bowing parameter b. The bowing parameter represents the magnitude of the second order correction to the linear dependence. For quaternary $In_xAl_yGa_{1-x-y}N$ alloy the energy band gap can be written as [22]

$$E_g(x,y) = xE_{g,InN} + yE_{g,AlN} + (1-x-y)E_{g,GaN} - b_{Al}y(1-y) - b_{In}x(1-x). \quad (2.3)$$

Here b_{Al} and b_{In} are the bowing parameters related to Al and In composition, respectively. The bowing of $Al_yGa_{1-y}N$ can be modeled with a static bowing parameter b_{Al} [23, 24]. In-containing alloys are more complex to model, because the bowing parameter b_{In} is believed to depend strongly on the In and Al content [22, 25]. Commonly used values for b_{Al} and b_{In} in hexagonal III-N alloys are listed in Table 2.3.

Table 2.3. Band bowing parameters b_{In} and b_{Al} for AlGaN, InGaN, InAlN and InAlGaN alloys. The b values marked with * depend on composition.

$Al_xGa_{1-x}N$

Al content (x)	b_{Al} (eV)	Ref.
$0 \leq x < 0.45$	0.69 $\pm$0.45	[24]
$0 \leq x \leq 1$	1	[23]

$In_xGa_{1-x}N$

In content (x)	b_{In} (eV)	Ref.
$0 \leq x \leq 0.5$	1.4	[26]
$x \leq 0.12$	3.5	[27]
$0 \leq x \leq 1$	3.5 - 0.9 *	[22]

$In_xAl_{1-x}N$

In content (x)	b_{In} (eV)	Ref.
$0 \leq x \leq 0.85$	6 - 1 *	[22]
$0.25 \leq x$	3	[28]

$In_xAl_yGa_{1-x-y}N$

In content (x)	Al content (y)	b_{In} (eV)	Ref.
$0.1 \leq x \leq 0.2$	$y < 0.2$	3*	[22]
0.03	$0.2 < y$	17*	[22]

To understand III-N heterostructures it is necessary to know the band offsets of binary III-N semiconductors. In all III-N heterojunctions the band alignment is of type I, in which the band gap of the lower energy semiconductor lies completely inside the band gap of the other. This is depicted in Fig. 2.4 in the case of AlN, GaN and InN. The valence band offsets are from Ref. 29.

2.3 Quantum wells

A quantum well is a thin layer that can confine carriers into two dimensions. In semiconductors this is obtained by fabricating a heterostructure where material with a specific band gap is sandwiched between layers of material with a wider band gap.

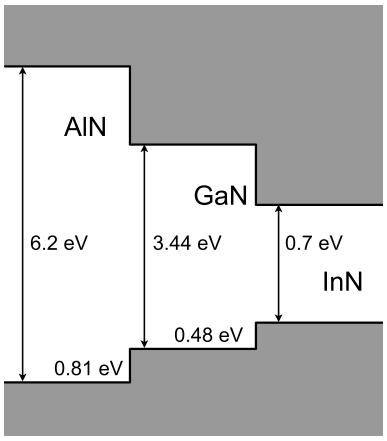

Figure 2.4. Band alignment of AlN, GaN and InN.

Fig. 2.5 a) shows the energy band diagram of an InGaN/GaN quantum well (QW) structure without polarization effects. It can be shown that if the quantum well thickness is comparable to the *de Broglie* wavelength of the carriers the energy within the well becomes quantized in discrete levels [30]. The main factors affecting the energies of the quantized levels are the potential wall height and the well width.

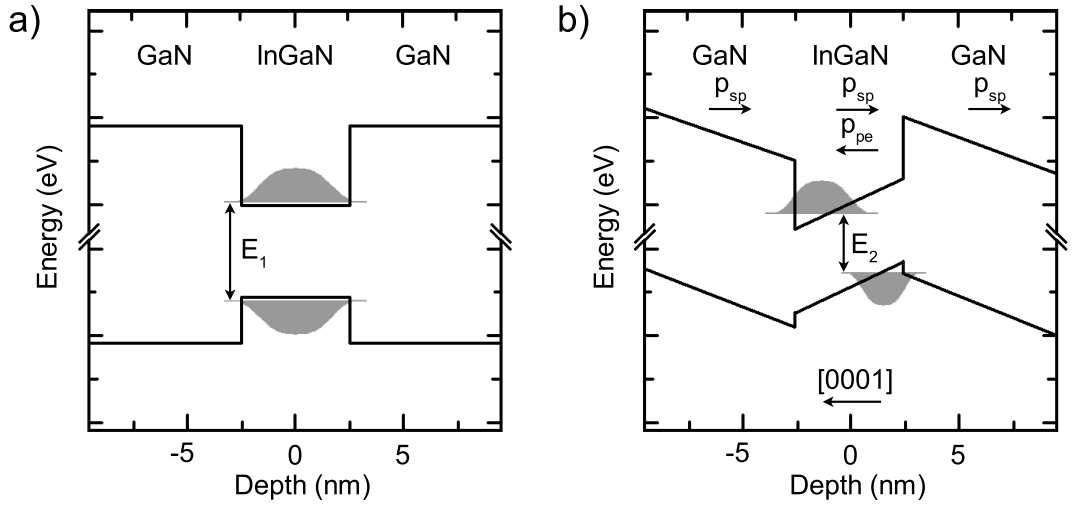

Figure 2.5. Schematic illustration of the energy bands of an InGaN/GaN QW a) without polarization effects and b) in the presence of spontaneous p_{sp} and piezoelectric p_{pe} polarization. Due to QCSE $E_1 > E_2$.

In quantum wells of III-N semiconductors both the spontaneous and the piezoelectric polarization described in section 2.1 play an important role. The magnitude of the internal electric field can be as high as 3.1 MeV/cm in an $In_{0.22}Ga_{0.78}N$/GaN QW structure [31]. Fig. 2.5 shows the directions and the effect of the spontaneous and piezoelectric polarizations on the band structure of InGaN/GaN QW. In the InGaN

QW the direction of the piezoelectric polarization is opposite to the spontaneous polarization and changes the potential well shape into triangular. The electron and the hole wave functions are shifted into the opposite sides of the QW and the difference of the electron and hole energy levels compared to the field-free structure is reduced. This reduction is seen as redshift of the emission wavelength and is known as quantum confined Stark effect (QCSE) [32]. The spatial separation of the electron and hole wave functions causes also reduction in the radiative recombination efficiency [33].

As the direction of the polarization is <0001>, the polarization is perpendicular to the QW plane when the QW is parallel to the (0001) c-plane. When the QW plane is parallel to the $(11\bar{2}0)$ a-plane the polarization also is parallel to the QW plane, and no QCSE or spatial separation of electron and hole wave functions is observed [10]. Therefore, films grown on c-plane are commonly called polar, and films grown on a-plane non-polar due to the presence or absence of the internal polarization, respectively. All the samples in this work were grown on c-plane surfaces, and are thus polar.

3 Experimental

In this chapter the experimental fabrication and characterization methods used in this thesis are presented.

3.1 Metalorganic Vapor Phase Epitaxy

In epitaxial growth the lattice structure of the underlying crystal, commonly called the substrate, is copied into the growing layer. The main tools used in epitaxial growth of semiconductor materials are molecular beam epitaxy (MBE) and metalorganic vapor phase epitaxy (MOVPE). The MOVPE method was developed in the late 60's by Manasevit *et al.* [34], but due to complex processes involving chemistry and hydrodynamics the evolution of the MOVPE technology was slow at the beginning. This situation has now changed and both MOVPE and MBE can now be used for growing thin films with sharp interfaces on the atomic level. Due to several improvements in the MOVPE technology it is now the main tool in both research and commercial production of III-N thin films. In the late 80's and early 90's modifications were made to the design of existing MOVPE tools to prevent harmful precursor prereactions [4], reactor flows were altered by utilizing a subflow of inert gas perpendicular to the substrate [1, 35] and *in situ* monitoring technique was developed to monitor film growth in real time [1, 35]. These modifications greatly improved the crystal quality and electrical properties of the MOVPE grown III-N films.

In MOVPE metalorganic precursors in gas phase are used to fabricate thin films. The precursors decompose thermally and the growth reaction takes place at the interface of the gas phase and the heated substrate. The reaction atmosphere is commonly nitrogen or hydrogen which are also used as carrier gases for the precursors. A gas flow diagram of the MOVPE system used in this work is presented in Fig. 3.1. The liquid metalorganic precursors are located in steel cylinders called bubblers, which are kept in temperature controlled baths. Accurate temperature control of bubblers is needed, since the vapor pressures of precursors are extremely sensitive to temperature. When carrier gas is passed through a bubbler, it is saturated with gaseous metalorganic material. In this system trimethylgallium (TMGa), trimethylindium (TMIn), trimethylaluminum

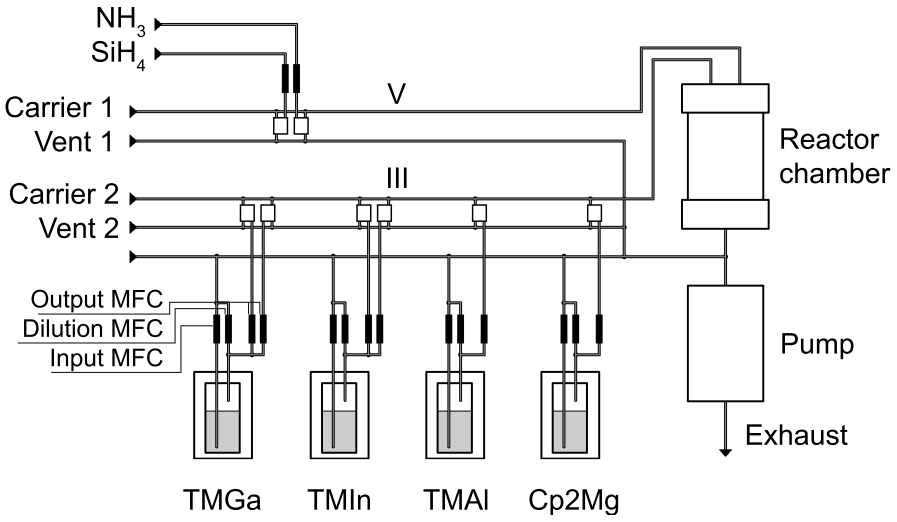

Figure 3.1. Gas flow diagram of the MOVPE system used in this work.

(TMAl) and bis-cyclopentadienylmagnesium (Cp_2Mg) were used as gallium, indium, aluminum and magnesium sources, respectively. The gas flows are regulated with valves and mass flow controllers (MFCs) into the reactor. A desired concentration of the precursor materials is achieved by changing the gas flow ratio of the input and dilution MFCs. The input MFC controls the gas flow through the bubbler, and the dilution MFC the flow bypassing the bubbler. Two separate output MFCs are used in the TMGa and TMIn lines to enable fast changes in TMGa and TMIn concentrations. This is needed for abrupt QW interfaces. In this system gaseous ammonia (NH_3) and silane (SiH_4) were used as nitrogen and silicon sources, respectively. A separate pipework is used for group-III (TMGa, TMIn, TMAl) and group-V (NH_3) precursors in order to minimize prereactions.

Fig. 3.2 shows a detailed image of the close coupled showerhead (CCS) reactor chamber. The group-III and group-V precursors enter the reactor chamber separately through the showerhead which provides uniform gas flow over the susceptor area. The gases mix only above the graphite susceptor surface which significantly reduces prereactions of the precursors. The SiC coated susceptor is heated from underneath by a tungsten heater coil up to 1500°C. Three 2" substrate wafers are located in the susceptor pockets. The ratio of the vertical and horizontal gas flows relative to the substrate is controlled by rotating the susceptor during operation. The pressure of the reactor chamber is controlled in the range of 50–900 Torr by a vacuum pump connected to the exhaust.

The description of the MOVPE growth process can be divided into thermodynamic, kinetic, hydrodynamic and mass transport aspects. The driving force of the reaction is defined by thermodynamics, kinetics control the rate at which reactions occur. Hydrodynamics describe the flow transport of precursor materials to the substrate

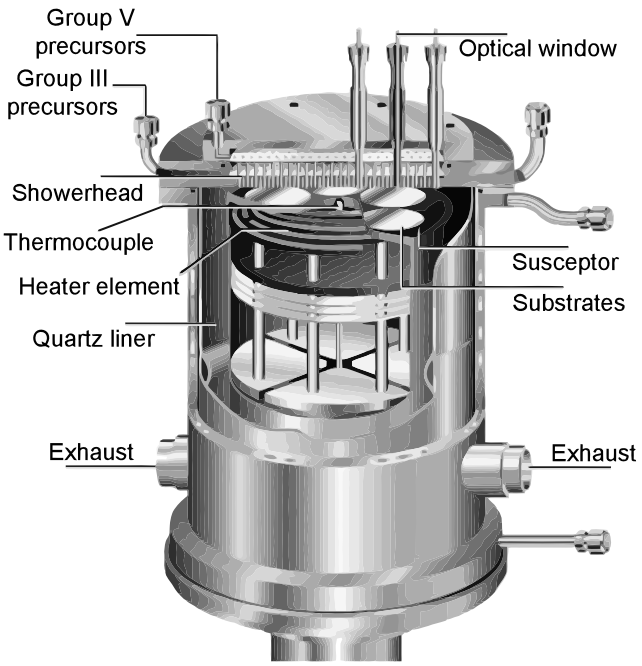

Figure 3.2. Schematic figure of the CCS reactor of the MOVPE system used in this work [36].

and mass transport defines the diffusive transport across the boundary layer [37]. The MOVPE growth of III-N materials will be discussed in more detail in chapter 4.

3.2 Reflectometry

The optical window of the reactor chamber (see Fig. 3.2) gives an access to monitor the substrates during the growth process. The *in situ* reflectometry setup used in this work is illustrated in Fig. 3.3. A broadband light beam is directed through a beam splitter and into the reactor chamber through the optical window. The light hits the samples perpendicular to the sample surface and is reflected back to the beam splitter. The reflected light is guided through an optical fiber to a band pass filter which selects a narrow measurement band from the broadband reflection. In this work a measurement wavelength of 638 nm was used. The narrow band measurement signal is directed onto a photodetector which is connected to a measurement computer. A trigger signal from the rotating susceptor is also connected to the computer. This allows the separate measurement of all the three wafers from a single optical port.

In the normal incidence geometry the reflectance of a single layer can be expressed as [38]

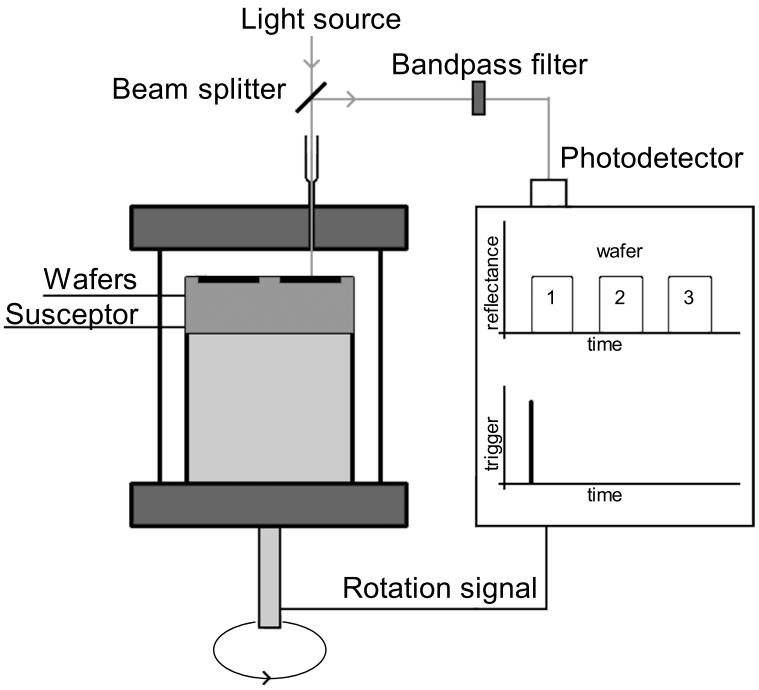

Figure 3.3. Schematic figure of the *in situ* reflectance measurement system used in this work.

$$R_0 = \frac{r_{12}^2 + 2r_{12}r_{23}cos(2\alpha) + r_{23}^2}{1 + 2r_{12}r_{23}cos(2\alpha) + r_{12}^2 r_{23}^2}, \quad \alpha = \frac{2\pi N_2 d}{\lambda}, \tag{3.1}$$

where r_{ij} is the reflectivity coefficient of the interface between materials i and j. N_2 and d are the refractive index and the thickness of the growing film and λ is the wavelength of the measurement signal. The notations of the reflectivity coefficient r_{ij} are shown in Fig. 3.4. The equation applies for non-absorbing films and smooth surfaces. The photon energy of the light is well below the absorption edge of the studied materials so the effect of adsorption can be omitted. However, the surface roughness needs to be taken into account. Small scale roughness can be modeled by introducing a Gaussian distribution of heights about the mean value [38]. The reflectance of a rough surface is given by

$$R = R_0 e^{-(4\pi\sigma)^2/\lambda^2}, \tag{3.2}$$

where R_0 is the reflectance of a smooth surface and σ is the root mean square surface roughness of the growing film.

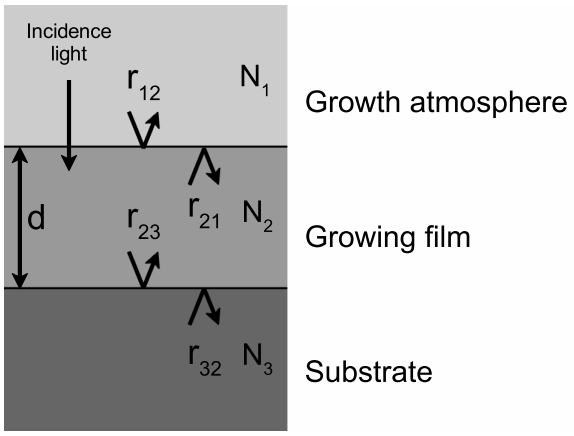

Figure 3.4. Reflections at the boundaries of the growth atmosphere, the growing film, and the substrate.

The magnitude of the reflected light oscillates during the growth of the film due to interference of light reflected at the surface of the film and the film/substrate interface. The growth rate of a film can be calculated from the oscillation period of the measured signal using Eq. 3.1. Since the oscillation period τ of reflected light is 2α the growth rate is given by

$$GR = \frac{\lambda}{2N_2\tau}. \tag{3.3}$$

3.3 X-Ray diffraction

Diffraction of X-rays in matter can be understood by means of the reciprocal lattice and the Laue condition. Mathematically the reciprocal space is a Fourier transformation of the electron density distribution. As the electrons are confined near the atomic cores, the reciprocal lattice is directly related to the lattice structure of the sample. The Laue condition defines the condition of constructive interference. Constructive interference occurs if the change in the scattered and incident wave vectors $\vec{k_s}$ and $\vec{k_i}$ is equal to a reciprocal lattice vector. The diffraction can be depicted by the Ewald construction shown in Fig. 3.5. The change in the wave vectors $\vec{k_s}$ and $\vec{k_i}$ defines the scattering vector $\vec{q}$. The angles ω and 2θ define the angle of the sample and the detector relative to the X-ray source.

A schematic drawing of the Philips X'Pert high resolution X-ray diffraction (HR-XRD) system used in this work is illustrated in Fig. 3.6. A four crystal germanium monocromator is used to select the Cu-$K\alpha_1$ line ($\lambda = 1.541$ Å) from the X-ray tube emission. A X-ray mirror is utilized between the monocromator and

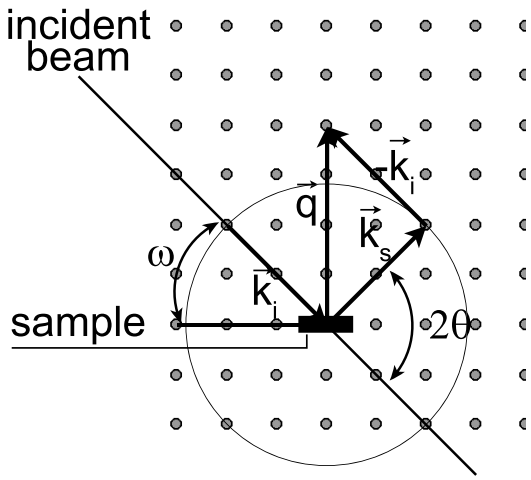

Figure 3.5. Ewald construction of X-ray diffraction.

the X-ray tube in order to reduce the divergence of the incident beam. The sample is mounted on a stage that can be rotated about all the axes marked in Fig. 3.6. The diffracted beam is passed through an analyzer which enhances the measurement resolution. Rotation of axes corresponds to movement in the reciprocal space as marked in Fig. 3.5. By combining several measurements it is possible to obtain a two dimensional diffraction space map from an area of the reciprocal space.

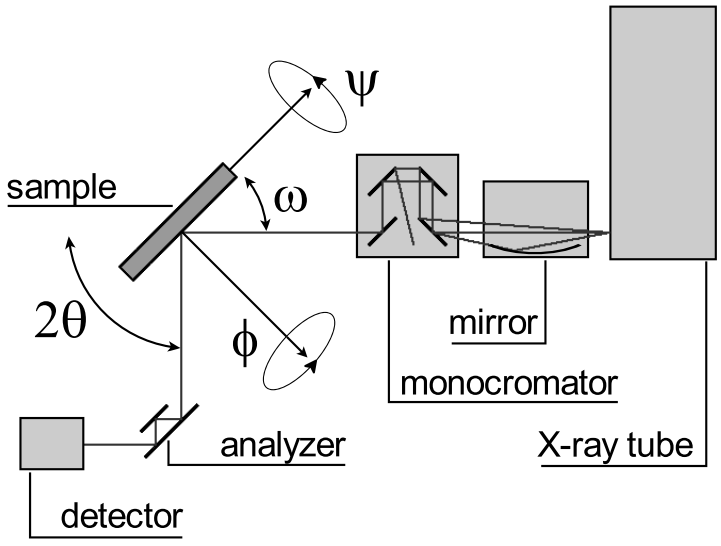

Figure 3.6. Schematic illustration of the HR-XRD measurement setup.

III-N semiconductor films can be described by the means of a mosaic model [39]. The model uses coherence lengths, tilt and twist to describe the structure of the crystal. Vertical and lateral coherence lengths can be thought as grain sizes in the

crystal, and tilt and twist describe the orientations of the grains with respect to each other. The origins of the mosaic structure in III-N films will be described in more detail in chapter 4.

3.4 Atomic Force Microscopy

Atomic force microscopy (AFM) is a type of scanning probe microscopy, in which the morphological properties of the sample surface are measured with a probe. The method is nondestructive and fast, as it requires very little preparation and the measurements can be done at room temperature and in ambient air. The operating principle of the AFM system used in this work is shown in Fig. 3.7. A sharp probe tip is attached to a flexible cantilever. As the sample is moved in respect to the tip Coulombic or van der Waals forces between the tip and the sample surface cause the cantilever to bend. A laser beam is reflected from the cantilever and detected by a dual-photodiode. A feedback loop controls the vertical position of the sample holder keeping the laser beam reflection at the same position. A computer gathers the feedback data and converts it to height information of the sample surface.

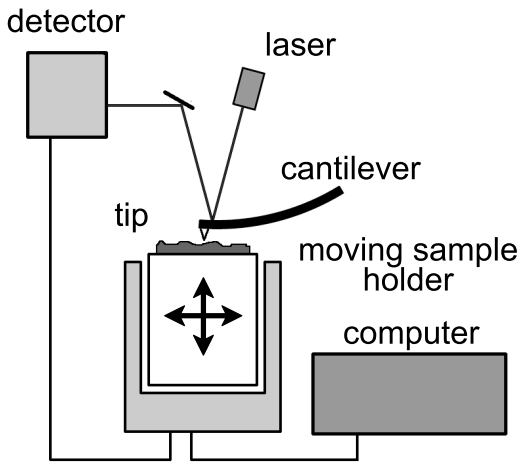

Figure 3.7. Schematic illustration of the AFM measurement setup.

In this work a NanoScope E AFM was used in contact mode. The vertical resolution of the system was 0.1 nm, so even a single monolayer step can be imaged. The lateral resolution depends on the type of the tip and the condition of the sample surface, and is typically a few tens of nanometers.

AFM was used to characterize the surface morphology and to determine the etch pit density (EPD) of the samples. In EPD measurements a selective etch is used to reveal dislocations on the sample surface [40]. The etch rates of different crystallographic orientations in the vicinity of dislocations at the surface differ [41].

This leads to the formation of pits on the dislocation sites. These pits can be imaged by AFM and so the dislocation density can be determined. In this work a 1:1 mixture of hot (240°C) sulphuric (H_2SO_4) and phosphoric (H_3PO_4) acids was used as the selective etch.

3.5 Optical spectroscopy

The optical properties of the samples were characterized by photoluminescence (PL) and electroluminescence (EL) measurements. PL is a commonly used method where carriers are generated by exciting the sample with photons of sufficient energy. The generated carriers recombine either radiatively or non radiatively at the energy states near the band edge. The spectrum of spontaneously emitted light is measured, and some electronic band properties and the optical quality of the sample can be determined. In EL measurements the carriers are excited by an external current source and transferred to the active region via n- and p-type layers.

In this work two types of PL setups were used. The InN samples in publication I were excited by using an argon ion laser (λ = 488 nm). The samples were cooled down using a closed cycle helium cryostat to 9 K. A nitrogen cooled Ge-diode was used as a detector. The InGaN/GaN and InGaN/InAlGaN samples in publications II, IV, and VII were excited at room temperature by using a He-Cd laser emitting at 325 nm. The maximum output power of the laser was 25 mW. An Ocean Optics USB2000 spectrometer was used as a detector.

4 MOVPE growth of III-N materials

This chapter gives a detailed review of MOVPE growth of III-N materials. Discussion is limited to growth of polar GaN on c-plane sapphire. Special attention is paid to the generation of dislocations at the GaN/sapphire interface. A multistep growth method for growth of low dislocation density GaN layers on sapphire is also presented.

4.1 Thermodynamics

In the MOVPE process thermodynamics define the driving force of the chemical reactions. In this section a thermodynamical analysis of binary GaN, InN and AlN growth is presented. In the analysis four incoming vapor species are considered: ammonia (NH_3), group three metalorganic (R_3III), hydrogen (H_2) and inert gas nitrogen (N_2). In the following equations gas phase is denoted by g and solid phase by s in parenthesis. A parameter F defines the ratio of H_2/N_2 in the reaction atmosphere. In the most simple approximation the group three metalorganic precursors can be assumed to decompose irreversibly [42, 43]

$$R_3III(g) + 3/2H_2(g) \rightarrow III(g) + 2RH(g). \tag{4.1}$$

In the CCS reactor used in this work the group-III and -V precursors are mixed only above the susceptor, so prereactions of the precursors can be omitted. By applying these assumptions the reaction governing the growth of III-N crystals can be written as [42, 43]

$$III(g) + NH_3(g) \leftrightarrow IIIN(s) + 3/2H_2(g). \tag{4.2}$$

This reaction is valid in the commonly used growth temperature range of 600–1100°C. As the reaction presented in Eq. 4.2 can proceed in both directions it describes both deposition and etching of a III-N film. As can be seen from Eq. 4.2

the introduction of excessive H_2 enhances the reverse reaction, *i. e.*, etching. The rate of decomposition varies drastically with the composition of the film and will be discussed later.

Thermodynamically, NH_3 is almost completely decomposed into N_2 and H_2 at temperatures higher than 300°C [43]. However, it is known that the decomposition rate of NH_3 under typical growth conditions is slow without a catalyst and the extent of decomposition depends on the growth conditions and equipment [44–46]. For the following calculations the effect of NH_3 decomposition is included in the parameter F.

Fig. 4.1 shows the calculated phase diagrams for the deposition of GaN, InN and AlN as a function of the partial input pressure of group-III species (P^0_{III}) and the V/III ratio. The three deposition modes (etching, droplet and growth) are marked for each material at several growth temperatures.

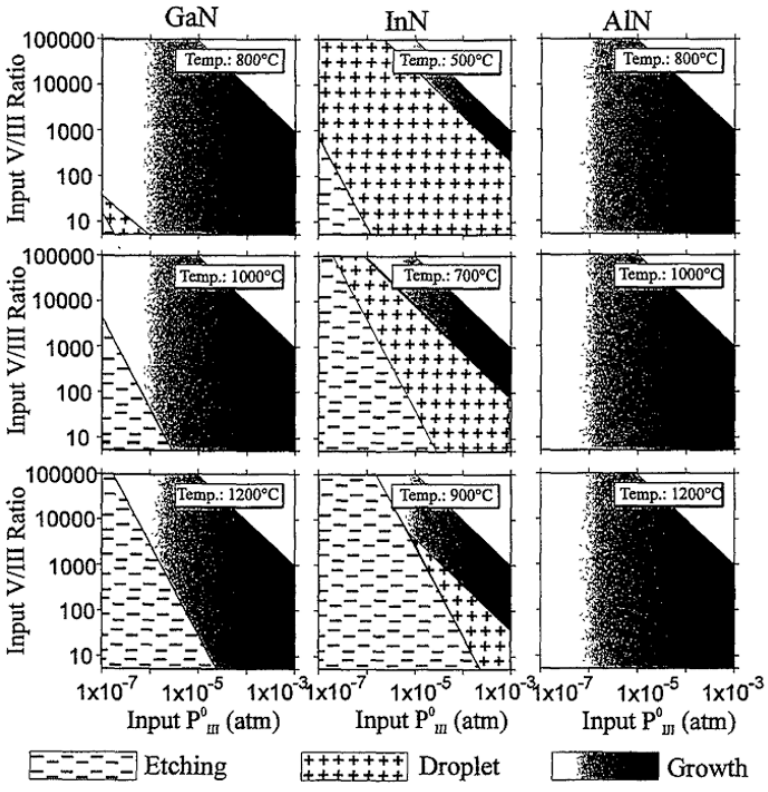

Figure 4.1. Calculated phase diagrams for the deposition of GaN, InN and AlN versus the input pressure P^0_{III} and V/III ratio [42]. In the calculations the total pressure was 1 atm and a value of 0.01 was used for F.

It can be seen from Fig. 4.1 that GaN and AlN can be grown under a wide range of growth conditions compared to the relatively small growth window of InN. In

the growth of InN the droplet mode is dominant at low temperatures and at high temperatures the area of etching is increased. As shown in Fig. 4.1 GaN and AlN can be grown at temperatures between 800°C and 1200°C, unlike InN which can be grown only in the range of 500–900°C.

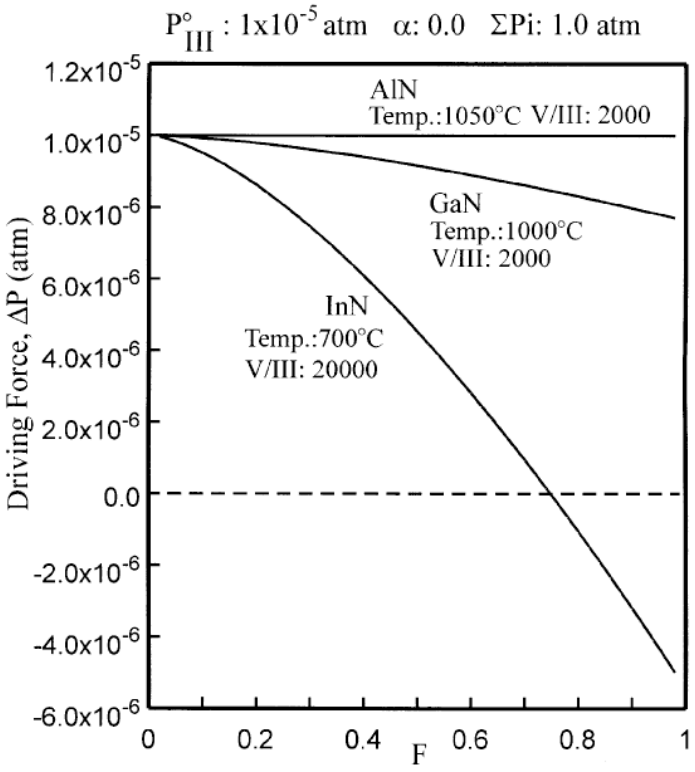

Figure 4.2. Driving force for the deposition of GaN, InN and AlN as a function of H_2/N_2 ratio F [43]. For deposition of AlN and GaN the effect of H_2 is small, whereas deposition of InN is highly sensitive to H_2 concentration.

The effect of hydrogen on the growth of GaN, InN and AlN is illustrated in Fig. 4.2. Here the ΔP is the driving force for the deposition. The driving force is defined as the deviation of group-III species input partial pressure from the equilibrium partial pressure. The values are calculated with typical growth parameters of GaN, InN and AlN. It can be seen from Fig. 4.2 that the driving force for the deposition of GaN and AlN exhibit little or no dependence on F. However, the driving force of InN decreases rapidly with increasing F and becomes negative at F=0.75. Therefore, it is necessary to use N_2 or a mixture of H_2 and N_2 during the growth of In containing nitrides. It should be noted that during the actual MOVPE growth of III-N materials H_2 is produced according to Eq. 4.2.

4.2 Growth of GaN

Since GaN crystals are currently not available in sufficient size and reasonable cost heteroepitaxial growth methods are required. Suitable substrate materials for hexagonal wurtzite GaN are silicon (111) surface, silicon carbide (SiC) and sapphire (Al_2O_3) [47]. Silicon substrates are promising since integration of III-N devices with Si electronics would open new possibilities in optoelectronics. However, the layers grown on (111) Si are often of poor quality and contain inclusions of cubic structure [48]. High quality GaN can be grown on SiC polytypes 4H and 6H [49]. The lattice mismatch of SiC with GaN is only 3.5 %, and SiC substrates have good electrical conductivity. The main drawback of SiC as a substrate is the large difference in thermal expansion coefficient in comparison to that of GaN, which leads to tensile stress in GaN films. Also the cost of 4H and 6H polytype substrates is high.

By far the most popular substrate for optoelectronic applications is c-plane (0001) sapphire. Sapphire substrates have good thermal stability and low cost. The drawbacks of sapphire, the large lattice mismatch with GaN (16 %) and the difference of thermal expansion coefficients of GaN and Al_2O_3, can be managed. GaN films grown on c-plane sapphire are polar and have (0001) plane parallel to sample surface as described in section 2.3. Also other orientations of sapphire can be used. GaN films grown on r-plane ($1\bar{1}02$) sapphire have a-plane ($11\bar{2}0$) orientation and are non-polar [50]. When grown on a c-plane sapphire the wurtzite GaN lattice is rotated 30° relative to the underlying substrate crystal to minimize stress. This results in a 16 % lattice mismatch between the GaN and sapphire lattices as illustrated in Fig. 4.3. All the samples in this work were grown on c-plane sapphire substrates. Therefore, the discussion is limited only to (0001) GaN films grown on c-plane sapphire.

Growth of GaN films was attempted initially directly on sapphire [52]. This resulted in polycrystalline films with a rough surface morphology. In 1986 a two-step growth method for growth of GaN was developed [4]. In this method a thin AlN layer was used between sapphire and GaN. The 50–100 nm thick AlN nucleation layer (NL) was grown at a lower temperature than the overgrown GaN layer. Also GaN can be used as a NL layer material [1, 51]. The use of two-step growth method increases significantly the material quality and improves the surface morphology. In this thesis GaN was used as a NL layer material.

Fig. 4.4 shows the surface reflectivity and corresponding surface morphologies during the two-step growth process. During the process H_2 is used as the carrier gas. The sapphire substrate is first annealed at 1100°C for the removal of impurities and nitridated at 800°C under NH_3 flow. During the nitridation a thin layer of AlN is formed on the surface [53]. The temperature is then reduced to 530°C and TMGa and NH_3 flows are switched on. TMGa and NH_3 react and an amorphous GaN NL is grown on sapphire. The NL growth is stopped at point 1 in Fig. 4.4 when

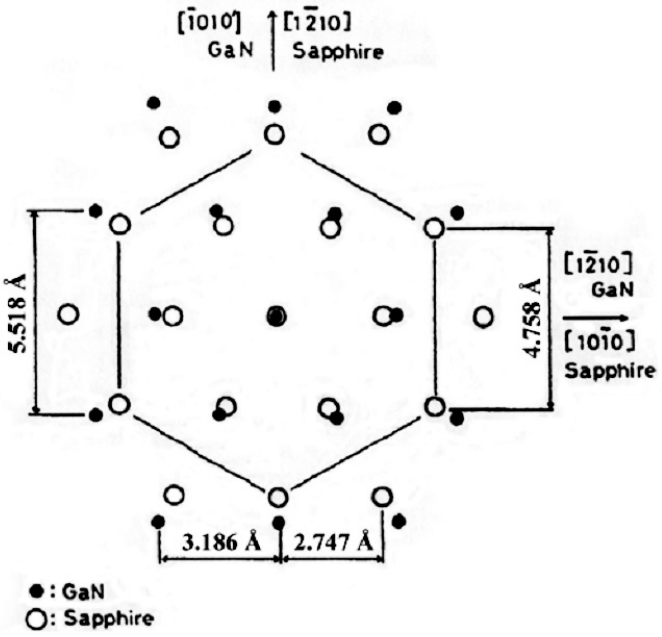

Figure 4.3. Epitaxial relationship of wurtzite GaN and c-plane sapphire [51].

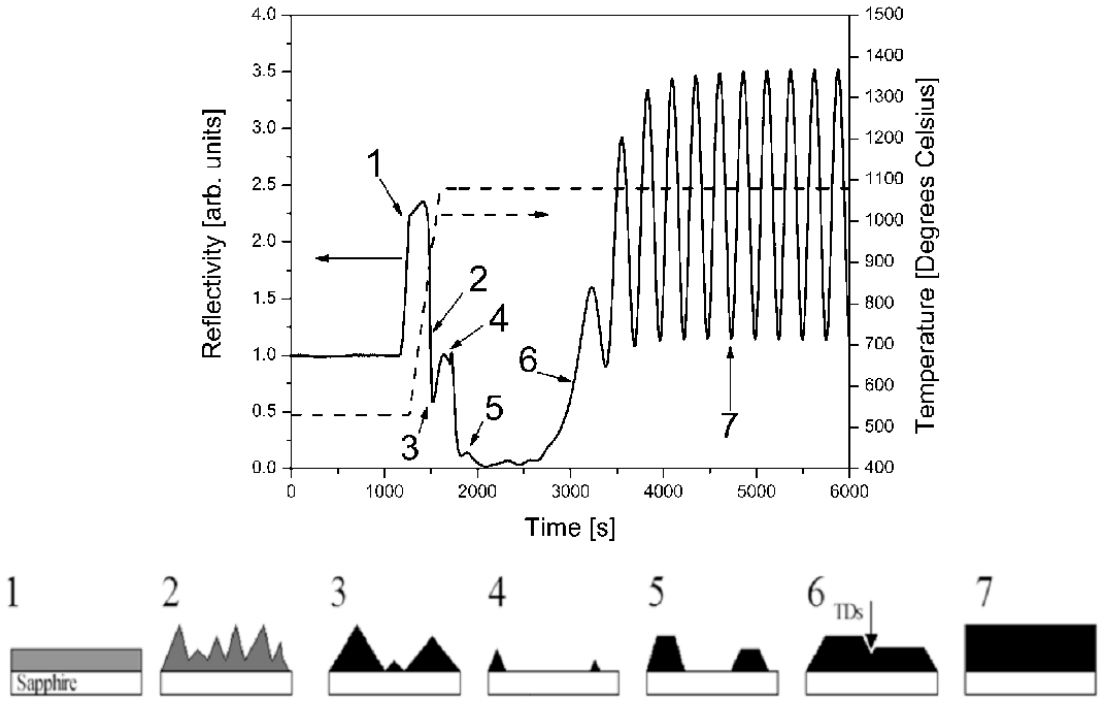

Figure 4.4. Illustration of the two-step growth process. The upper part presents reflectivity data obtained *in situ* during two-step growth. The lower part presents surface morphologies corresponding to points labeled in the reflectivity data [51].

the NL thickness reaches the desired value of 40–100 nm. The temperature is then ramped up to 1080°C and the recrystallization of the NL begins. The amorphous material partly decomposes [54], and a material redistribution process leads to the formation of GaN islands [55]. The use of hydrogen as the carrier gas increases the decomposition rate of the amorphous material. During this process the surface roughness is increased, as material is moved into nucleation islands (NIs) composed of hexagonal crystal structure [55, 56]. This can be seen as the rapid decrease of the reflection signal in Fig. 4.4 at point 2. At point 3 the material loss from the GaN islands leads to a partial exposure of the sapphire substrate and the reflection signal starts to increase. The NI size and density reaches the desired value at point 4 and high temperature (HT) GaN growth is started.

At the beginning of the HT growth the deposition occurs primary on the NIs that grow in size both laterally and vertically. The 3D growth of NIs decreases the reflectivity signal starting from point 4 until point 5. The coalescence of NIs occurs between points 5 and 6. As the NIs merge the surface becomes gradually smoother and reflectivity starts to increase. After full coalescence a smooth surface and 2D growth is achieved. This can be seen from the oscillations of the reflectivity signal (point 7).

4.3 Dislocations in GaN

By using the two-step growth method of GaN on c-plane sapphire the dislocation density of the films is typically in the range of 10^9–10^{10} cm^{-2} [51]. The threading dislocations (TDs) are generated mainly at the coalescence boundaries of adjacent NIs [56]. TDs accommodate the relative crystal misorientation of the NIs as they coalesce. In-plane twist between the NIs results in an edge component in the dislocations with the line direction along [0001] and tilt misalignment results in a screw component (Burgers vector along [0001]) in the dislocations [39, 57]. Depending on the different components present in the dislocations they can be either pure screw-, pure edge- or mixed-type threading dislocations. Generally TDs generated at the boundaries of NIs are edge-type, and dislocations starting inside the NIs are of screw- or mixed-type. As the misorientation of the NIs and, therefore, the TDs continue through the whole epitaxial film the resulting crystal can be described as a mosaic crystal [39]. This is illustrated in Fig. 4.5. TDs are known to cause detrimental effects on the device performance. TDs can act as non-radiative recombination centers [58] and reduce the lifetime of devices by acting as diffusion channels between the electrodes [59].

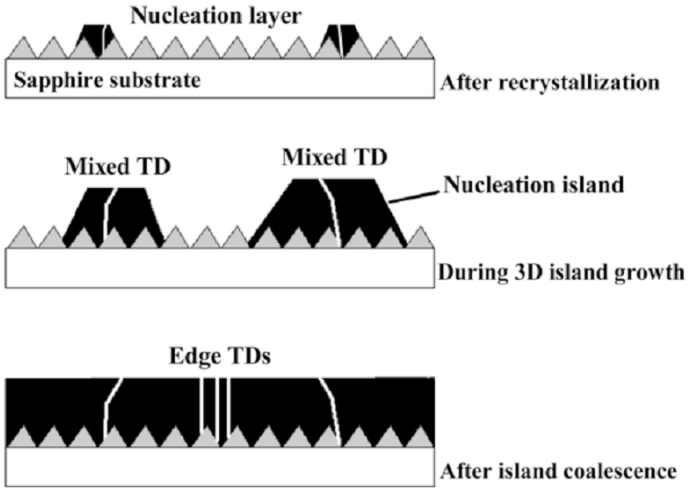

Figure 4.5. Generation of threading dislocations during GaN growth [51].

4.4 Multistep growth method

Several methods have been developed to reduce the TD density in GaN films grown on sapphire. In epitaxial lateral overgrowth (ELOG) an oxide mask is deposited on the grown GaN film surface. The oxide mask is patterned and used to expose parts of the underlying GaN layer. GaN growth is continued, and laterally grown sections of GaN are virtually free of dislocations [47, 60]. A major drawback of this method is that time consuming lithographic steps are required and the samples need to be removed from the reactor. Other method to reduce the TD density is to use SiN micromasking. In this method the principle is the same as in ELOG, but the SiN mask is deposited *in situ* using silane and ammonia as precursors. Nano-holes on the SiN layer surface provide nucleation sites for GaN overgrowth. The sticking coefficient of GaN on SiN is low causing the GaN film to grow over the SiN micro mask [61].

In this work a multistep growth method (MGM) was used to reduce the TD density of the grown GaN layers. In the MGM the density and the size of GaN nucleation islands is controlled *in situ* [51, 62, Publ. V, and Publ. VI]. By using the MGM a NI density as low as 1×10^7 cm^{-2} can be achieved. This results in the TD density of 5.0×10^7 cm^{-2} in the overgrown GaN film [Publ. V, VI].

In the MGM the NIs are grown by alternately depositing a thin layer of low temperature GaN and recrystallizing it at high temperature. The reflectometry data of a four cycle multistep process is presented in Fig. 4.6. The critical points of the reflectivity curve of one deposition step are labeled in the inset of Fig. 4.6. The film deposition at low temperature occurs between steps 1 and 2. During this time the reflection increases due to interference between the surface of the growing

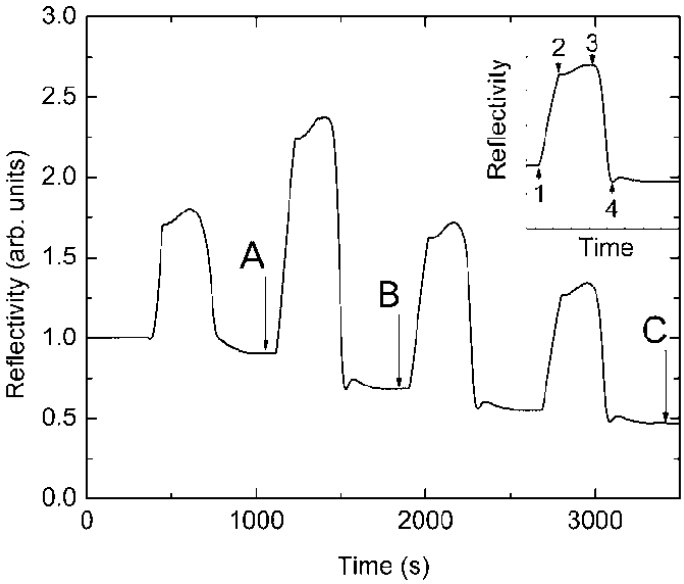

Figure 4.6. Surface reflectivity during the multistep growth of GaN nucleation islands [62].

amorphous GaN film and the GaN/sapphire interface. After the interruption of growth at point 2 the temperature is ramped up and the reflectivity is slightly increased due to the increase of GaN refractive index as a function of temperature. This increase continues until point 3 which marks the start of island formation. This happens around 900°C. The temperature is further ramped up until the reflectivity signal drops to the level at point 4. The temperature is then ramped down and the next deposition cycle is performed. The base level of reflectivity between deposition cycles is gradually decreased. This is due to the increase of GaN island size as shown in Fig. 4.7 a), b), and c). These figures are AFM surface scans of the sapphire substrate surface at points A, B, and C in Fig. 4.6, respectively.

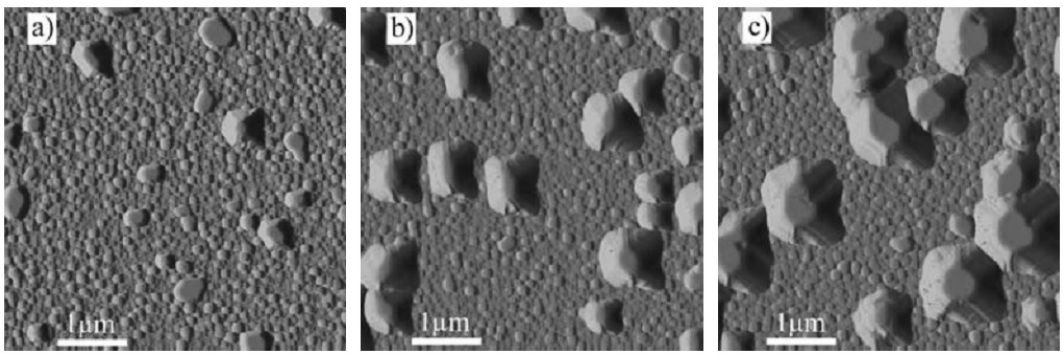

Figure 4.7. AFM data illustrating the surface morphology for the samples grown with one a), two b), and four c) multistep cycles. The images were taken in deflection mode [62].

The density of the NIs is governed by the deposition time of the low temperature nucleation layer [63]. In the MGM this is used as an advantage, as very thin NLs can be used and the size of the islands can be increased so that the islands act as efficient nucleation centers for high temperature GaN overgrowth. Control of the NL overgrowth is important, so that additional islands are not formed. This is done by optimizing the carrier gas flow rate and reactor pressure during the high temperature overgrowth of GaN islands.

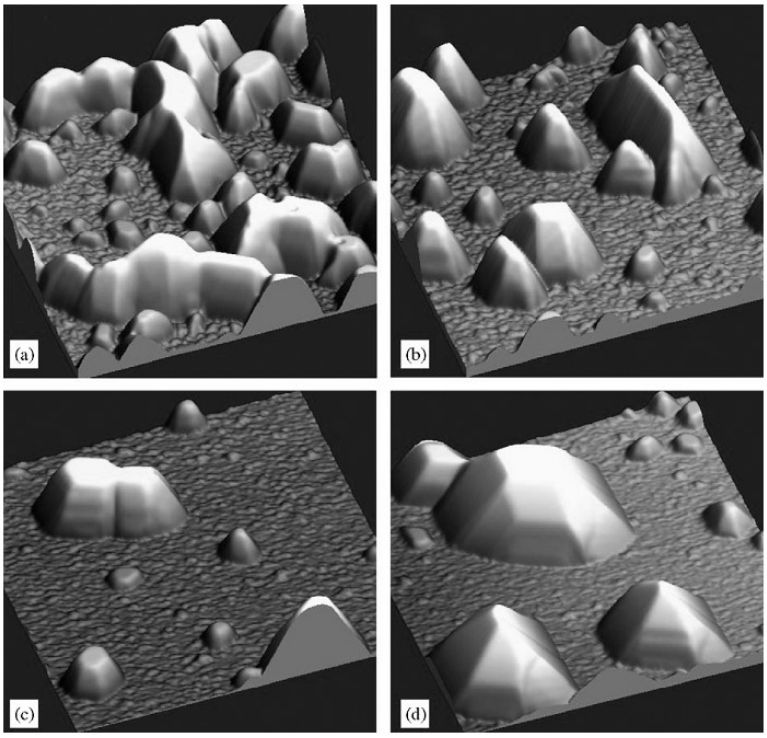

Figure 4.8. AFM data illustrating the nucleation between the NIs at the beginning of high temperature growth. The total H_2 flow rates, growth pressures and growth times were a) H_2 = 10.5 slm, P_g = 200 Torr, T_g = 300 s, b) H_2 = 10.5 slm, P_g = 400 Torr, T_g = 300 s, c) H_2 = 12 slm, P_g = 500 Torr, T_g = 300 s, and d) H_2 = 12 slm, P_g = 500 Torr, T_g = 700 s [Publ. VI].

Fig. 4.8 shows the effect of the carrier gas flow and reactor pressure on the overgrowth process GaN of NIs. The growth process of these samples consisted of first depositing a low density of NIs by the MGM, this corresponded to point C in Fig. 4.7. During overgrowth the total H_2 carrier gas flow rate and growth pressure were varied in the range of 10.5–12 slm and 200–500 Torr, respectively. It is clearly seen how the increase in reactor pressure reduces the nucleation between the NIs. No additional NIs are observed even with an overgrowth time of 700 s in Fig. 4.8 d). The increase in the reactor pressure enhances desorption of GaN in H_2 atmosphere [64], so desorption occurs primary on the thermally less stable material between the NIs [Publ. VI]. Desorption can be enhanced further by increasing the H_2 flow as was done in samples

shown in Figs. 4.8 c) and d). This increases the amount of reactive H_2 required for GaN decomposition [Publ. VI].

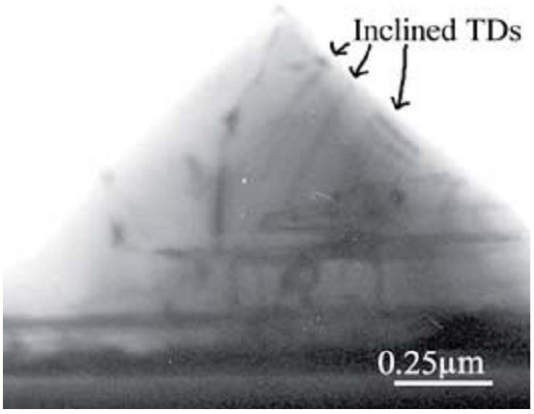

Figure 4.9. Cross-section TEM image of a NI overgrown with a low V/III ratio. TDs incline to become perpendicular to a high-index facet of the NI [Publ. V].

Dislocation density can be further reduced by using a low V/III ratio during the high temperature overgrowth of the NIs. The low V/III ratio causes TDs present in the NIs to incline from the [0001] direction and to turn perpendicular to the high index facets of the NI [Publ. V]. During the NI coalescence the inclined TDs have a higher probability to terminate or to combine with each other. The inclination of TDs is shown in a cross section TEM picture of a NI overgrown with low V/III ratio (Fig. 4.9).

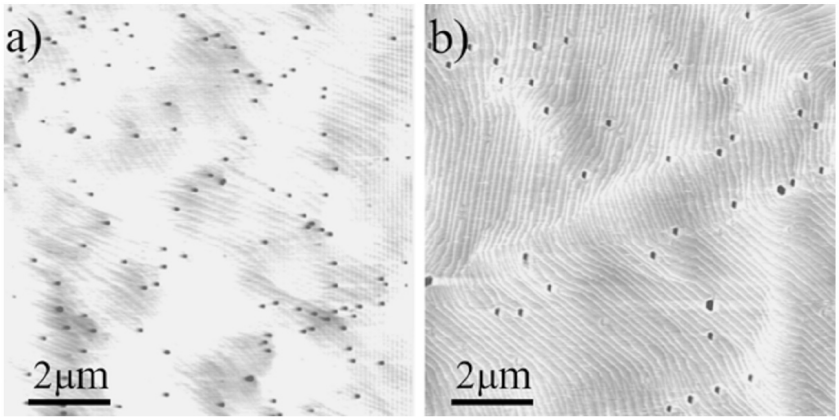

Figure 4.10. AFM data illustrating the EPD on GaN layers grown by a) the two-step method and b) the multistep method [Publ. V].

The high dislocation density of GaN films results mainly from the high density of nucleation sites generated during the growth of the NL [56, 57]. As the density of the NIs is decreased the TD density decreases roughly in the same proportion

[Publ. VI]. This is shown in Fig. 4.10 where the AFM data of selectively etched GaN layers grown by a) the two-step method, and b) the MGM is presented. The TD density on the sample grown by using the MGM is 5.0×10^7 cm^{-2} while TD density of 1.0×10^8 cm^{-2} was measured from the sample grown by using the two-step method. A low V/III ratio was used in both samples to stimulate the inclination of TDs in the NIs.

4.5 (In,Al)GaN compounds

In and Al containing GaN alloys are commonly used in III-N based optoelectronic devices. The bond energies between the group-III and N atoms vary over a large range, with E_b(Al-N) = 2.88 eV, E_b(Ga-N) = 2.22 eV and E_b(In-N) = 1.93 eV, in the binary nitrides AlN, GaN and InN [21]. Consequently, the thermal stability of group-III nitrides differ enormously. AlN and GaN have melting points of about 3200°C and 2500°C, while InN sublimates at temperatures above 550°C [65]. Therefore, typical MOVPE growth temperature of Al-containing GaN alloys is above 1000°C, while In-containing alloys are grown below 800°C. Furthermore, the lattice mismatch between AlN and GaN is about 3.5 % while the mismatch between GaN and InN is as high as 10 %.

In the growth of Al-containing alloys difficulties rise from the high Al-N bond strength. Due to the high adsorption energies the surface mobility of the absorbed Al species is low. Also the probability of harmful pre-reactions increases [66]. The surface mobility can be increased by increasing the growth temperature and reducing the V/III ratio [67]. Pure AlN is commonly grown at temperatures of 1300–1600°C [68].

The growth temperature of In-containing alloys is limited from above by thermal decomposition of the films [65], and from below by the reduced reaction rate of NH_3 at low temperatures [69]. The maximum In content depends mainly on the growth temperature and growth rate [70]. High growth rate reduces In desorption from the surface [71]. Due to the low reaction rate of NH_3 an extremely high V/III ratio is needed. The optimum growth parameters vary between different reactor types, since the reactor geometry has been found to affect the reaction rate of NH_3. In the CSS reactor the reaction rate of ammonia is enhanced in the temperature range of 550–650°C [Publ. I]. Despite the relatively weak In-N bond energy InN films often grow in 3D mode caused by the low surface mobility of In species [72, and Publ. I]. The relatively weak In-N bond may also cause indium surface segregation and formation of metallic In droplets in InN and InGaN films [73, and Publ. I]. When grown on GaN, a composition-pulling effect along the growth axis has been observed in InGaN films that involves the rejection of indium atoms from the InGaN lattice to the film surface [74, 75]. As a result of these effects, InGaN layers usually become progressively In-rich as the thickness of the layer increases.

Quaternary InAlGaN films are especially interesting for strain engineering in quantum well structures and in UV-emitting devices, as both the lattice parameter and the band gap can be altered [76, 77]. Also the optical quality of films is usually high due to the defect insensitive properties of In alloys [10, 11]. However, MOVPE growth of InAlGaN films is challenging due to the different optimum growth parameters of In- and Al-containing alloys as described above. Films with In content below 0.15 and Al content below 0.4 have been grown [9, 78, and Publ. IV]. Typically a growth temperature of 750–875°C and growth pressures in the range of 100–770 Torr are used. Both affect the InAlGaN film quality strongly [79]. MOVPE growth of InAlGaN films will be discussed in more detail in section 6.3.

Recently the properties and growth of ternary AlInN compound have been under a considerable study [80]. AlInN with In content of 0.18 is lattice-matched to GaN and can be used to realize nearly strain-free structures for photonic and electronic applications [80]. However, the different optimum MOVPE growth conditions of In- and Al-containing films make growth of AlInN a challenging task. Phase separation and compositional inhomogeneities in the grown films currently limit the use of AlInN material in devices.

5 GaN LEDs

This chapter gives an overview of a typical GaN LED structure and its properties. The focus is on MOVPE growth of the multilayer LED structures for green, blue and near UV emitters. Also the LED structure used in this work is presented.

5.1 Overview

LEDs are often cited as the ultimate solid-state light sources [81]. Conventional light sources, such as filament light bulbs and fluorescent lamps depend either on incandescence or discharge in gases. These processes are accompanied by large energy losses. When compared to conventional light sources the major benefits of LED light sources can be summarized as follows: energy savings caused by improved efficiency, environmental benefits resulting from durability and long life time, and greater control of emission properties allowing customizing of emission for specific purposes [82]. Recent advances in high brightness LED technology have increased the efficiency of LEDs sufficiently to enable their use in general lighting applications [83].

GaN-based LEDs operating in the green to near-UV range are commercially available. Also current white LEDs employ a GaN based blue or near-UV LED that is coated with a phosphor [1, 84]. The external quantum efficiency of GaN-based blue LEDs can be as high as 38 %, and luminous efficacy of white lamps manufactured from blue LEDs as high as 96 lm/W has been reported [85]. For comparison the luminous efficacy of common conventional light bulbs and fluorescent lamps are 20 lm/W and 70 lm/W, respectively. The output power of GaN-LEDs shows only a weak dependence on ambient temperature unlike conventional III-V LEDs [86] and the lifetime of white LEDs exceeds 50 000 h at room temperature [87].

5.2 Structure of III-N LEDs

A schematic figure of a typical blue GaN-based LED is shown in Fig. 5.1. A GaN buffer layer is grown on sapphire as described in section 4.2. The actual LED

structure consists of a n-doped GaN layer, an active region, an electron blocking layer, and a p-doped GaN layer. The n-doped GaN layer is typically 2 μm thick and doped with silicon. Typical carrier concentration in the n-layer is in the order of 1×10^{19} cm^{-3} [1].

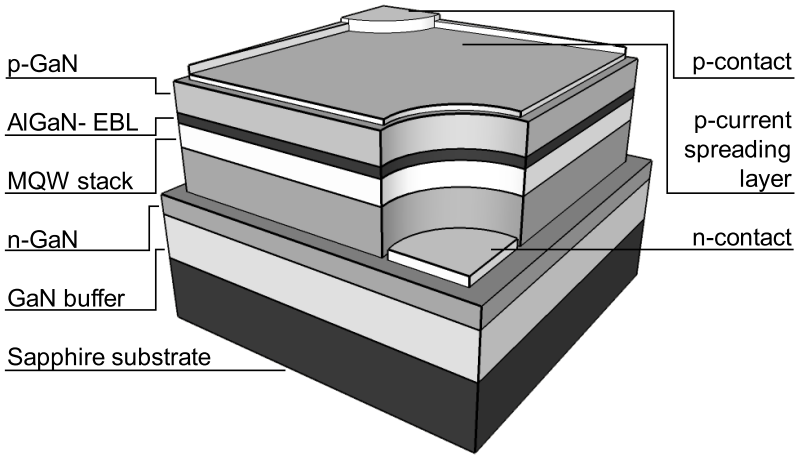

Figure 5.1. Schematic illustration of a typical GaN LED structure.

The active region of the LED consists of an InGaN/GaN multiple quantum well (MQW) stack. The InGaN QW width is practically limited to a maximum of 5 nm due to the spatial separation of electron and hole wave functions caused by the piezoelectric polarization [88]. The emission wavelength is determined by the concentration of In in the QWs and also by the thickness of the QWs due to the QCSE [33]. In blue LEDs the In content is around 10 %, while in green LEDs In content is around 20 % [Publ. III]. Growth of the MQW stack is problematic since the InGaN QWs need to be grown at temperatures below 900°C. GaN barriers grown at such temperatures exhibit rough surface morphology which can deteriorate the optical quality of the MQW stack [Publ. II]. Growth and properties of the InGaN/GaN MQW stack will be discussed in more detail in sections 6.1, 6.2, and 6.5.

Magnesium (Mg) is commonly used for p-type doping of GaN. Fabrication of high quality p-type conducting layers is a challenging task due to passivation of Mg acceptors by H_2 during the growth of the layer [89, 90]. The Mg acceptors are activated by thermal annealing after growth, and p-type conductivity is achieved [91]. Typical carrier concentration in the p-type layers is in the range of 1–5 $\times$ 10^{17} cm^{-3} [1, 91]. As the carrier concentration in the p-type layer is one order of magnitude smaller than in the n-type layer, the overflow of electrons from the n-GaN to p-GaN reduces the efficiency of the device. An AlGaN electron blocking layer (EBL) is used to confine the electrons in the active region [92]. The EBL layer is doped with Mg in order to facilitate the transportation of holes into the active region [92].

As the n-type layer resides inside the LED structure and no electric connection is possible through the sapphire substrate, etching is needed in order to fabricate an electric n-contact. The etching is done by dry etching of GaN. Inductively coupled plasma (ICP) can be used to etch the lateral sidewalls of the LED mesas [93]. A metallic contact is then deposited on the n-layer for electric n-contact. Due to the poor conductivity of the p-type layer a thin semitransparent current spreading layer is deposited on the top surface of the LED mesa. To further improve the current uniformity in the active region, the p-contact has fingers that spread the current along the edge of the contact area.

Near-UV LEDs in the wavelength range of 370–400 nm can also be grown on GaN buffers and employ InGaN QWs [8]. The QW thickness and In content is reduced compared to blue emitting LEDs. The reduction of the QW thickness reduces the QCSE, and the emission peak is shifted to shorter wavelengths [33]. The reduction of the In content in the InGaN QWs reduces also the potential well depth of the QW and the efficiency of the device. To compensate the reduction of the potential well, Al is added to the barrier layers [8]. However, the growth temperature of the barriers is limited due to the low thermal stability of the InGaN wells, and the quality of AlGaN layers grown at low temperatures is low [94]. The quality of low temperature grown AlGaN layers can be enhanced significantly by introducing a small amount of In into the layers [94, 95]. The MOVPE growth of high quality InGaN/InAlGaN MQW structures for emission at 380 nm will be discussed in more detail in section 6.3.

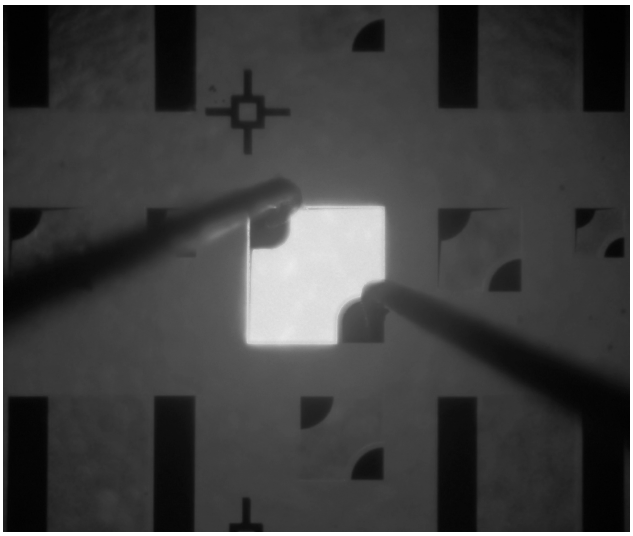

Figure 5.2. Blue LED fabricated at Department of Micro and Nanosciences, TKK, operating at 20 mA current.

Fig. 5.2 shows a top view of a blue LED fabricated for this work operating at 20 mA current. The LED chip was grown by MOVPE and processed at the Department of Micro and Nanosciences. The multistep method was used to grow a low dislocation

density GaN buffer on sapphire on which the LED structure was deposited. The layer structure of the LED is illustrated in Fig. 5.1. The active region of the device consists of a ten pair InGaN/GaN MQW stack with QW and barrier thicknesses of 3 and 25 nm, respectively. The In content of the QWs is 0.12. The MQW stack is covered by a 20 nm thick AlGaN EBL with an Al content of 0.2, and a 200 nm thick p-GaN layer. MOVPE growth and properties of such LEDs are discussed in more detail in the next chapter.

6 InGaN/(InAl)GaN quantum wells

In this chapter MOVPE growth and properties of InGaN/(InAl)GaN QW structures for LED applications are discussed. The influence of InGaN/GaN MQW stack surface morphology and the effect of TDs on the optical properties of QWs and the performance of LEDs is described. MOVPE growth of quaternary InAlGaN layers and InGaN/InAlGaN MQW structures is discussed and an InGaN/InAlGaN MQW structure emitting at 383 nm is presented. Finally, origins of the high efficiency of InGaN QWs are reviewed.

6.1 MOVPE growth of InGaN/GaN quantum wells

Growth of high quality InGaN/GaN quantum wells is a crucial step in fabrication of high brightness near-UV, blue and green LEDs. The growth parameter window of high quality InGaN/GaN MQW structures is small due to the different optimum growth conditions of GaN and InGaN films as presented in chapter 4. The most important parameters for growth of InGaN films are the growth temperature and the growth rate [96]. The growth temperature allows one to control the composition of the InGaN layers and determine the luminescence properties of the InGaN/GaN MQW stack to a large extent. The growth temperature also determines the maximum growth rate at which high quality InGaN films can be grown [96]. Too high a growth rate results in deteriorated crystal quality and poor optical performance. A QW with In content in the excess of 0.15 is required for fabrication of blue and green LEDs. For such a high content a growth temperature below 900°C is needed. Also nitrogen is used as the carrier gas during growth of the MQW stack in order to facilitate In incorporation in the QW layers. On the other hand, high quality GaN is typically grown at temperatures in excess of 1000°C, and in H_2 ambient. When grown in N_2 the surface morphology and crystal quality of GaN is deteriorated [97].

When a constant temperature and N_2 ambient is used during growth of the InGaN/GaN MQW stack, the surface of the GaN barrier located on top of the MQW stack is characterized by the presence of pits with inclusions in the center of the pits [98, 99, and Publ. II]. The pits, also known as V-defects, are formed at the ends of TDs due to strain induced mechanisms and/or by anisotropy of growth rate of different crystallographic planes within the growing InGaN QW layer [100–105, and

Publ. II]. Inclusions embedded into these V-pits are related to the presence of In-rich clusters that have nucleated at the point where the TDs intersect the InGaN/GaN interface [106]. The subsequent low temperature growth of GaN barrier, on top of a InGaN QW, causes 3D nucleation of GaN at the In-rich cluster located at the apex of the V-pit [106]. During the barrier growth the inclusion, consisting primarily of GaN, propagates through the barrier leading to rough QW/barrier interfaces and non-planar surface of the uppermost GaN barrier layer. This can be seen as sharp peaks located at the center of V-pits in Fig. 6.2 a). The V-defect and the resulting inclusion disturb growth of the subsequent QWs and the size of the V-pits is increased as the low temperature growth of the MQW stack is continued. This is seen in a transimission electron microscopy (TEM) image of the InGaN/GaN MQW stack in Fig. 6.1. When the MQW stack is capped by GaN grown at high temperature smooth surface morphology is recovered.

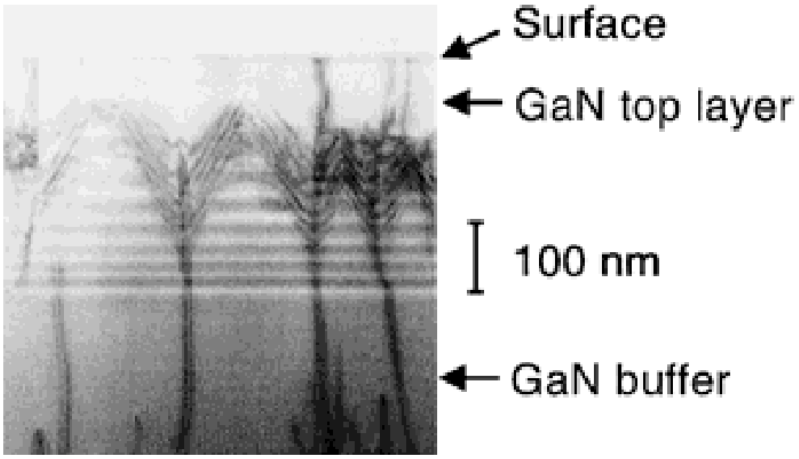

Figure 6.1. TEM image showing V-defects formed at the TD/QW intersection point in an InGaN/GaN MQW stack [107]. The InGaN/GaN MQW stack is covered by a 100 nm thick GaN layer grown at a high temperature. In the image InGaN layers are seen as light horizontal lines and TDs as dark vertical stripes.

Various growth techniques have been developed to obtain smooth planar morphology and sharp interfaces within the InGaN/GaN stack. Growth of barriers at elevated temperatures [107], growth of GaN barriers in the presence of H_2 [106, 108], and growth interruption (GI) after the QW growth [108, 109] are believed to be the most effective approaches for improving the surface morphology of InGaN/GaN quantum structures. A high growth temperature should promote 2D growth mode and the regrowth of V-defects without the formation of inclusions. Growth interruption and the presence of H_2 should suppress the density of In-rich clusters and prevent the formation of inclusions.

In this work the effect of these growth techniques was evaluated by growing a number of 5-period InGaN/GaN MQW samples on top of GaN buffer layers. The InGaN

layers were grown with TMIn/(TMIn+TMGa) molar flow ratio of 0.7 at temperature of 745°C with N_2 as a carrier gas. Pressure was set at constant 300 Torr. The thickness of InGaN layers was 3 nm with targeted In content of 0.15. The GaN barrier thickness was fixed at 10 nm. In the reference sample A1 the GaN barriers were grown with the same parameters as the InGaN QWs. The effect of the barrier growth temperature was tested by increasing the growth temperature of the GaN barriers to 900–960°C. In these samples the InGaN QWs were covered prior to the GaN barrier growth by a 2 nm thin GaN capping layer, grown at the QW growth temperature. The temperature was then ramped up, and the GaN barrier was grown. The effect of GI was tested by stopping growth for 5–50 s after the deposition of GaN barriers at 900°C. During this time the samples were annealed in N_2 atmosphere. The effect of hydrogen was evaluated by growing the GaN barriers at 900°C with H_2/N_2 carrier gas flow ratio of 0.02–0.2. A thin capping layer grown at the QW growth temperature was used also in all of the GI and hydrogen samples.

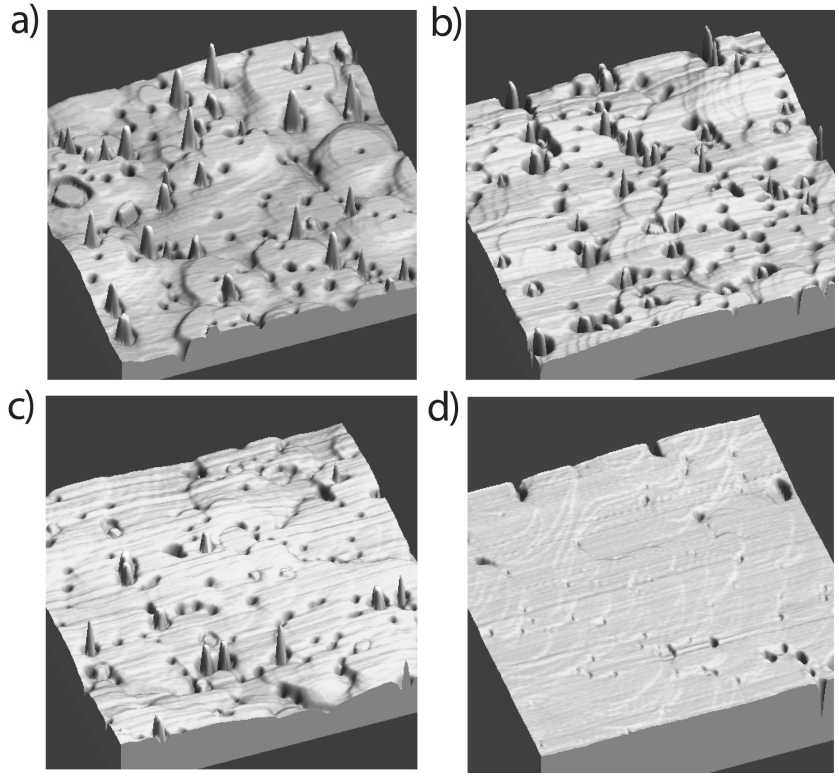

Figure 6.2. 3×3 μm^2 AFM surface scans of the samples: a) carrier gas during barrier growth: N_2, $T_{barrier}$=745°C (sample A1); b) carrier gas during barrier growth: N_2, $T_{barrier}$=900°C; c) carrier gas during barrier growth: N_2, $T_{barrier}$=900°C, GI 20 s; a) carrier gas during barrier growth: H_2/N_2=0.02, $T_{barrier}$=900°C. The height scale in all the figures is 20 nm [Publ. II].

The surface morphology of the samples grown with various growth techniques is shown in Fig. 6.2, and the PL emission measured from the samples is shown in

Fig. 6.3. As mentioned, in the sample A1 the surface of the topmost GaN barrier is non-planar and several V-pits with inclusions located inside the pits are seen. The luminescence peak from the QWs is at 480 nm and full width half maxima (FWHM) of the peak is 23 nm. In addition there exists a long-wavelength shoulder at 500 nm.

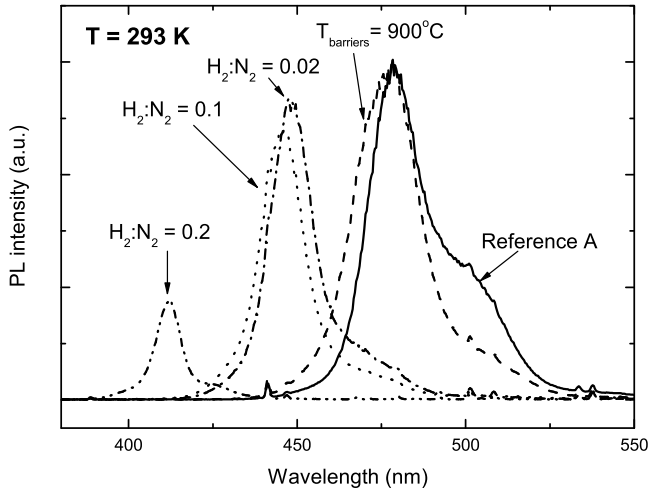

Figure 6.3. PL spectra of InGaN/GaN MQW samples grown with different GaN barrier growth procedures. Solid line - reference sample A1, dash line - GaN barriers grown at 900°C, dash-dot line H_2/N_2 ratio 0.02, dot line - H_2/N_2 ratio 0.1, dash-dot-dot line - H_2/N_2 ratio 0.2 [Publ. II].

Increasing the barrier growth temperature to 900°C eliminates neither the pits nor the inclusions as shown in Fig. 6.2 b). However, the surface outside the pits is smoother, and the long-wavelength shoulder is removed from the PL spectrum (see Fig. 6.3). As the inclusions are unaffected by the elevated barrier growth temperature, the long-wavelength shoulder seen in the PL spectrum of sample A1 is thought to result from fluctuations of In content in the QWs. Increasing the growth temperature of the barriers causes partial evaporation of In and results in more uniform composition in the QWs. The negligible effect of the elevated growth temperature on the surface morphology of the MQW stack indicates that the temperature is still too low to achieve complete removal of the In-rich clusters and to eliminate the inclusions. Further increase of the barrier growth temperature resulted in planar surface morphology, but the optical quality of the QWs was severely degraded.

By increasing the GI time from 5 s to 20 s the number of inclusions and consequently the number of In-rich clusters was gradually decreased. The surface morphology of a MQW sample grown with a 20 s GI in shown in Fig. 6.2 c). The decrease of

the inclusion density did not affect the PL spectra of the samples at all. However, increasing the GI time to 50 s caused severe degradation of optical quality, but no improvement in the surface morphology.

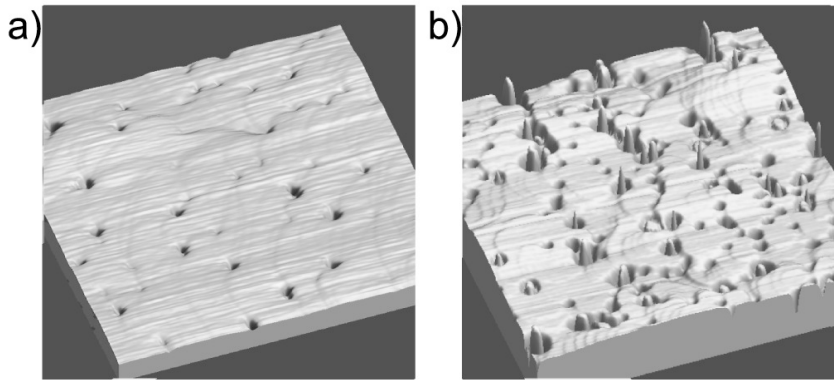

Figure 6.4. 3×3 μm^2 AFM surface scans of the MQW samples with an In content of 0.15 in the QWs. The GaN barriers of the samples were grown with a carrier gas flow ratio of a) H_2/N_2=0.02 and b) H_2/N_2=0 (sample B1). The height scale in both of the figures is 20 nm [Publ. II].

As can be seen from Fig. 6.2 d), using a H_2/N_2 carrier gas mixture of 0.02 during growth of GaN barriers completely removes the inclusions, and a smooth surface is obtained. Hydrogen is believed to remove the In-rich clusters from the QW/barrier interface via enhanced desorption and thus prevent the formation of the inclusions [106]. Along with improved morphology the H_2 causes a 30 nm blue shift of the PL emission peak position (see Fig. 6.3). This is due to H_2 induced reduction of the average In content in the InGaN QWs. Further increase of the H_2/N_2 ratio did not lead to any improvement in morphology, but when the ratio of 0.2 was used the optical quality of the sample was deteriorated (see Fig. 6.3).

The effect of introducing H_2 during the barrier growth was verified by growing a sample pair with an In content of 0.15 in the QWs, one with H_2/N_2 carrier gas ratio of 0.02 during barrier growth and one with pure N_2 (reference sample B1). The growth temperature of the QWs in the sample grown with H_2 was reduced by 15°C to compensate the loss of In caused by H_2. The surface morphologies of the samples are shown in Fig. 6.4. It can be seen that all the inclusions are removed and smooth surface morphology is obtained by using a H_2/N_2 carrier gas flow ratio of 0.02 during barrier growth. As the In content of the samples is the same, it can be safely concluded that the elimination of the inclusions is due to the H_2 induced removal of In-rich clusters from the InGaN/GaN interface. Improved layer periodicity and interface quality of the MQW stack can be observed also from the HRXRD (0002) $\omega - 2\theta$ diffraction curves of the samples (Fig. 6.5). In the XRD diffraction curve of the sample grown with H_2 the higher order satellite peaks are stronger and more pronounced, compared to the reference sample B1. This is clear

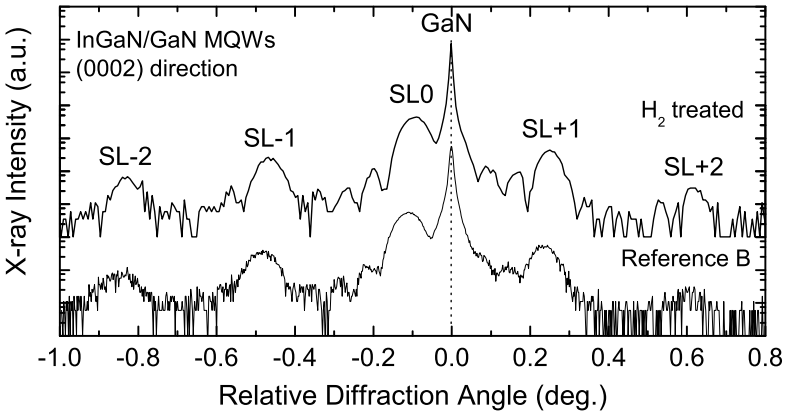

Figure 6.5. HRXRD (0002) ω-2θ diffraction curves of MQW samples with an In content of 0.15 in the QWs. The GaN barriers of the samples were grown with a carrier gas flow ratio of a) H_2/N_2=0.02 (H_2 treated) and b) H_2/N_2=0 (reference sample B1) [Publ. II].

evidence of improved structural quality of the MQW stack. However, no difference is seen in the PL performance of the samples.

To further examine the effect of the GaN barrier morphology on the performance of the InGaN/GaN QWs a series of blue, green, and near-UV LED structures was grown. The MQW stack of the LED samples consisted of 10 pairs of 3 nm thick InGaN QWs and 25 nm thick GaN barriers. The growth temperature of the InGaN QWs was varied to achieve an In content between 0.05 and 0.18. The corresponding EL peak wavelengths ranged from 400 nm to 500 nm. The GaN barriers were grown at the temperature of 920°C and with a H_2/N_2 carrier gas ratio of 0.2. This type of MQW growth process of blue and green LEDs resulted in the relaxation of the structure during growth of the MQW stack or the p-GaN layer over the stack. This was observed as a decrease of the oscillation amplitude and reflection signal intensity of the *in situ* reflectometer and was verified by HRXRD. In the near-UV LEDs growth of the barriers with the presence of H_2 did not improve the performance of the LEDs. On the contrary, the FWHM of the EL peak increased by 20 %. The relaxation of the layer structure in the blue and green LEDs during growth occurred most likely due to build up of strain in the MQW stack, as the In content and thus the compressive strain in the QWs higher in than in the near-UV LEDs.

The relaxation could be prevented by decreasing the number of QWs in the MQW stack or by employing strain control techniques, such as placing an InGaN underlying layer below the MQW stack [110, 111] and introducing In to the barriers [71, 112]. However, as the surface morphology of the MQWs had only a minor effect on the PL intensity of the samples, the effect on the LED performance is questionable.

It can be concluded that the inclusions have very little effect on the optical properties of the InGaN/GaN QWs. Even though smooth morphology of the InGaN/GaN structures did not improve the optical quality or the performance of the MQW or LED structures, it could be beneficial for other properties. For example the structural quality of the active region may affect the lifetime of LEDs and laser diodes. Also plasmonic coupling of InGaN QWs and silver nanoparticles has been reported [113–115]. The surface plasmon fringing field penetration depth in GaN is only 40 nm [115], and therefore a smooth surface morphology of the InGaN/GaN MQW stack is required.

6.2 Influence of TDs on InGaN/GaN quantum wells

By optimizing the growth process of the InGaN/GaN MQW stack the inclusions could be removed, but the V-defects were left intact. To clarify the formation of the V-defects a sample pair with an identical 5 period InGaN/GaN MQW stack was grown on two GaN buffers with different TD densities. The GaN barriers of the MQW stack were grown at 900°C and by using a H_2/N_2 carrier gas ratio of 0.02 to achieve smooth morphology. For the reference sample A2 a regular two-step growth method was used to grow the GaN buffer for the MQW stack as described in section 4.2. The two-step growth method resulted in the TD density of 6×10^8 cm^{-2} in the GaN buffer. For the sample B2 the multistep growth method was used to grow the GaN buffer layer. This resulted in the TD density of below 1×10^8 cm^{-2}. These dislocation densities were confirmed by measuring the EPD by AFM on the etched GaN buffer layers (see Fig. 6.6 a) and b)). The AFM scans of the surfaces of the MQW samples A2 and B2 are shown in Figs. 6.6 c) and d), respectively. As can be seen from Fig. 6.6, the amount of V-pits present on the MQW structure surface is correlated with the EPD density of the buffer layer. The amount of V-pits on the surface of sample B2 is significantly smaller than on sample A2.

The formation of the V-pits on the MQW stack surface can be explained by examining the initial growth mechanism of In-containing alloys. In the growth of In-containing III-N alloys even small surface perturbations, such as threading dislocations, cause anisotropic growth of the film [100, 101, 104]. In the case of threading dislocations the dislocation cores tend to grow into inclined facets [100, 104]. The slowest growing $(1\bar{1}01)$ crystal planes form the sidewall facets of the pits as shown in Fig. 6.7. The pits grow in size as the thickness of the film is increased and In incorporation into the faceted areas is increased [74]. This results in a strongly inhomogeneous In composition, and has a profound effect on the emission mechanism in the InGaN QWs [11]. This will be discussed in more detail in section 6.5.

However, the reduction of TD and V-pit density by nearly an order of a magnitude did not have any effect on the PL emission measured from B2 compared to the

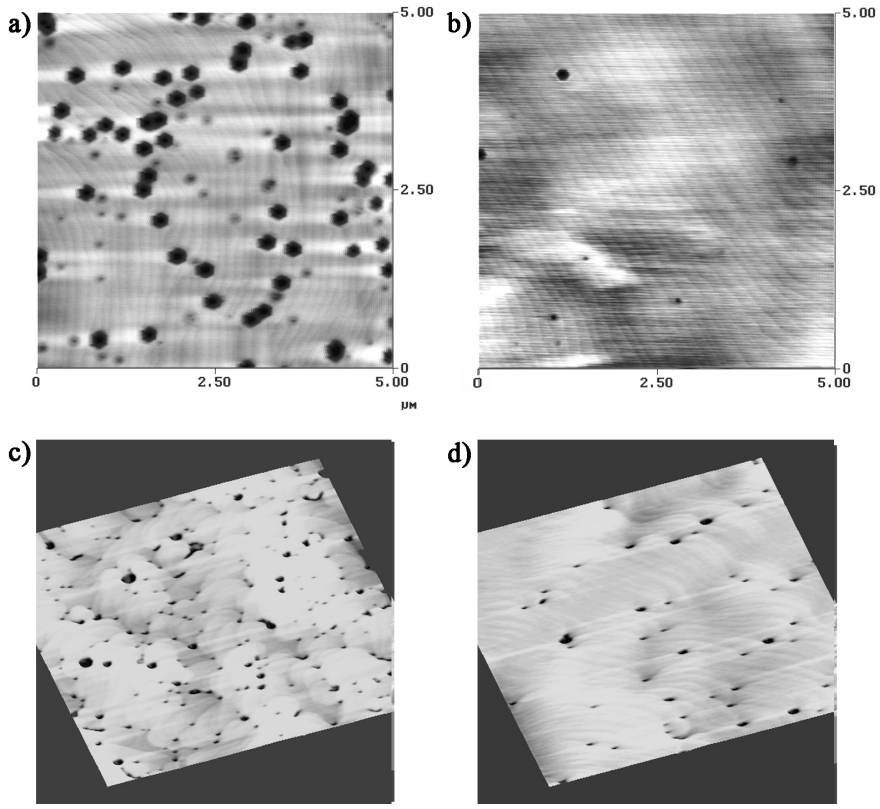

Figure 6.6. 5×5 μm^2 AFM surface scans of etched GaN buffer layer surfaces used for the growth of MQW structures with a) TD density of 6×10^8 cm^{-2}, and b) below 1×10^8 cm^{-2}. The surface of the MQW structures grown on c) high TD density buffer (sample A2), and d) low TD density buffer (sample B2). The height scale in all the figures is 20 nm [Publ. II].

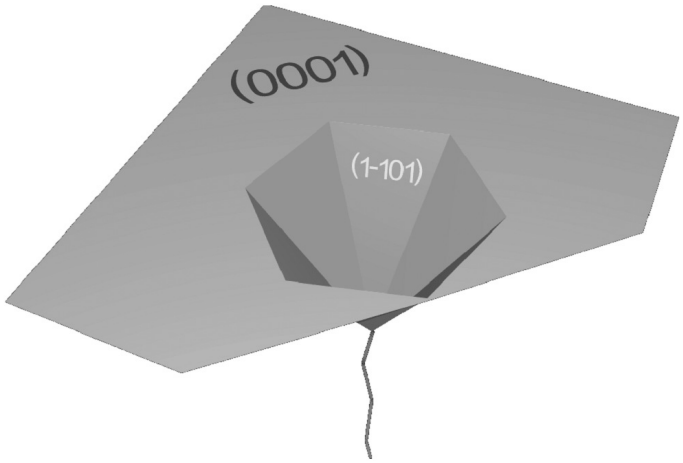

Figure 6.7. Schematic illustration of a hexagonal V-shaped pit emerging at the apex of a threading dislocation in a InGaN heterostructure [11].

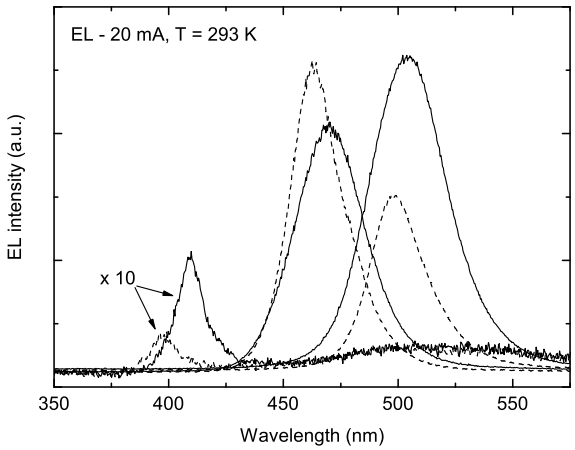

Figure 6.8. Electroluminescence spectra of the LEDs grown on two-step buffer (straight line) and on low TD density multistep buffer (dashed line) [Publ. III].

reference sample A2. This suggests that the TDs and the resulting V-pits have little effect on the optical properties of the InGaN QWs. This was further studied by growing a series of InGaN/GaN LED structures on two-step GaN buffers with a TD density of 6×10^8 cm^{-2} and on multistep GaN buffers with a TD density of 7×10^7 cm^{-2}. The MQW stack of the LED samples consisted of 10 pairs of 3 nm thick InGaN QWs and 25 nm thick GaN barriers. The growth temperature of the MQW stack was varied from 800°C to 875°C to achieve an In content between 0.05 and 0.18, corresponding to EL peak wavelengths from 400 nm to 500 nm. The sample series consisted of near-UV (400 nm), blue (460 nm) and green (500 nm) LED structures grown both on high and low dislocation density GaN buffers. Fig. 6.8 shows the EL spectra measured from the LEDs operating at a current of 20 mA. It can be seen that the emission from the LEDs grown on multistep buffers is blueshifted by 10 nm and the FWHM of the emission peak is decreased by about 20 % compared to the LEDs grown on two-step buffers. The intensity of the blue LED grown on the multistep buffer is increased by 30 % when compared to the similar structure grown on two-step buffer, while the intensities of the near-UV and green LEDs grown on multistep buffer are decreased by 40 % and 60 %, respectively. The blueshift observed in the LEDs grown on multistep buffers is due to the increased compressive strain in the InGaN QWs caused by the reduced dislocation density in the buffer layer. As a similar LED structure was used for near-UV, blue, and green LEDs, the poor performance of the near-UV LEDs is most likely due to non-optimal MQW structure for short wavelengths. The potential well of the QWs is shallow as the In-content in the QWs of the near-UV LEDs is only 0.05. A more suitable MQW structure for near-UV emission is presented in section 6.4.

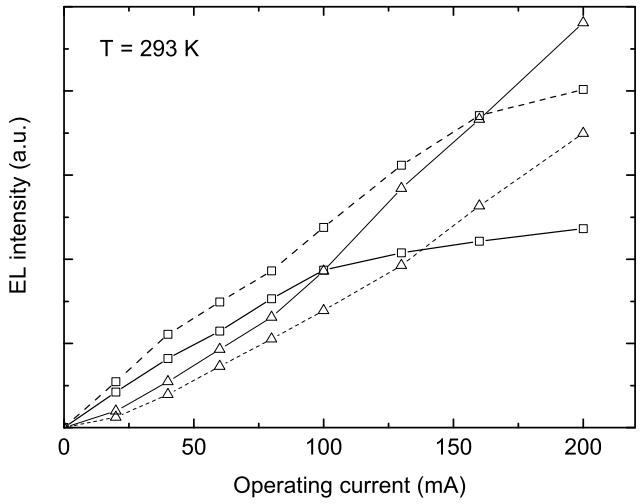

Figure 6.9. Electroluminescence intensity of blue (squares) and green (triangles) LEDs grown on two-step (solid line) and on multistep (dashed line) GaN buffers as a function of operating current [Publ. III].

Fig. 6.9 shows the EL intensities of the blue and green LEDs grown on two-step and multistep GaN buffers as a function of operating current. Saturation of the EL intensity is observed in the both blue LEDs at high current. The saturation threshold of the blue LED grown on two-step GaN buffer is 100 mA, while the threshold of the blue LED grown on multistep buffer is 150 mA. This corresponds to current densities of 10 A/cm^2 and 15 A/cm^2, respectively. In addition to the increase in the EL saturation current the blue LED grown on the multistep GaN buffer showed a 70 % higher maximum EL output power at an operating current of 200 mA. No saturation of the output power was observed in the green LEDs grown on two-step buffer or on multistep buffer. This indicates that the recombination mechanism of the InGaN/GaN MQW structures depends strongly on the excitation level and on the In-content of the QWs. This will be discussed in more detail in section 6.5.

6.3 MOVPE growth of InAlGaN films

In UV and near-UV emitting III-N structures a better carrier confinement is achieved by using AlGaN as a barrier material compared to GaN barriers. However, a large lattice mismatch and poor material quality of AlGaN films grown at low temperature limit the use of InGaN/AlGaN MQW structures [94]. The quality of AlGaN layers

grown at low temperature can be significantly increased by introducing a small amount of In to the layer [94, 95]. Furthermore, employing the quaternary InAlGaN alloy as a barrier material the strain state of the active InGaN layers can be varied between compressive, zero, and tensile strain [116].

In order to fabricate high efficiency InGaN/InAlGaN MQW structures emitting at near-UV, the effect of In content on the quality of $In_xAl_yGa_{1-x-y}N$ films was studied. For this a series of InAlGaN films was grown on sapphire substrates covered by a 2 μm thick GaN buffer layer. After growth of the GaN buffer layer the temperature was decreased to 850°C and the carrier gas was switched to N_2. A constant pressure of 300 Torr and a V/III ratio of 1100 were used during growth of the InAlGaN layers. TMGa and TMAl flows of 25 μmol/min and 51 μmol/min were used, respectively. The In composition was varied by changing the TMIn flow in the range of 0–46 μmol/min. The films thicknesses were roughly 100 nm in all the samples.

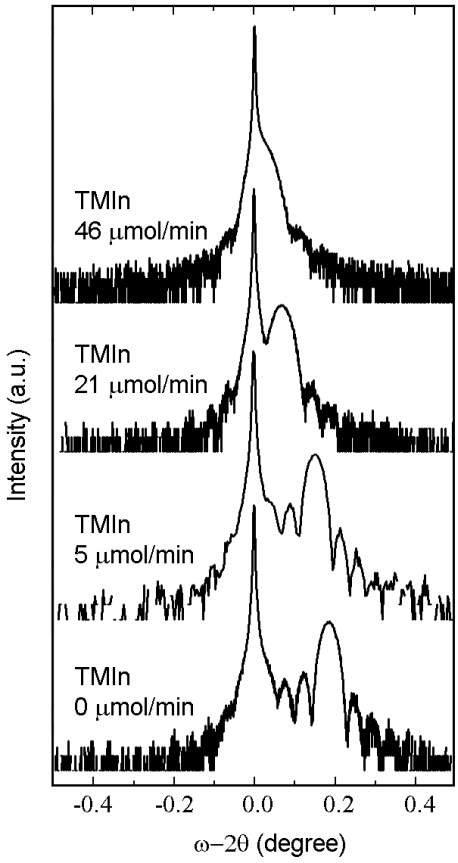

Figure 6.10. HRXRD (0002) ω-2θ diffraction curves of InAlGaN films grown with various TMIn flows [Publ. IV].

Fig. 6.10 shows the HRXRD (0002) ω-2θ diffraction curves of InAlGaN films grown with various TMIn flows. It can be seen that by increasing the TMIn flow the

InAlGaN peak is shifted closer to the GaN peak, and the InAlGaN film is almost lattice matched to GaN when TMIn flow of 46 μmol/min is used. The presence of multiple clear diffraction fringes indicates sharp InAlGaN/GaN interfaces. The FWHM of the InAlGaN peak is determined by the layer thickness.

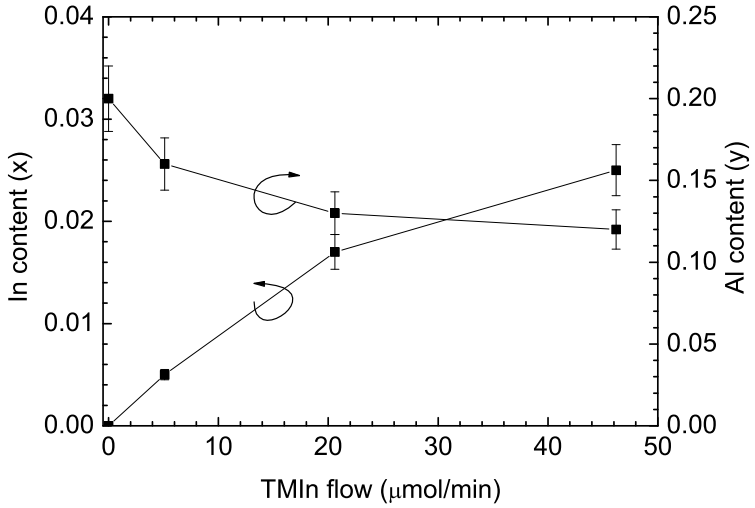

Figure 6.11. In and Al contents of $In_xAl_yGa_{1-x-y}N$ films as a function of TMIn flow [Publ. IV].

The In and Al content of the films were determined by combining HRXRD and secondary ion mass spectrometry (SIMS) measurements of the films. By using this method the In and Al contents can be evaluated with the relative accuracy of 10 %. Fig. 6.11 shows the In and Al contents as functions of TMIn flow. It can be seen that the TMIn flow affects both the In and Al contents of the films. The In content of the films increases and Al content decreases with increasing TMIn flow. The Al content of the films grown with the TMIn flow of 46 μmol/min was reduced by 40 % when compared to the films grown with the TMIn flow of 0 μmol/min.

The compositional SIMS depth profile of the InAlGaN samples grown with TMIn flows of 21 μmol/min or less show sharp interfaces and uniform In and Al compositions throughout the film. However, in the sample grown with the TMIn flow of 46 μmol/min, the Al content increases gradually from 0 to 0.12 during the first tens of nanometers starting from the InAlGaN/GaN interface, while the In content is uniform throughout the film. This can be seen in the case of InGaN/InAlGaN MQW structures in Fig. 6.14 b). The non uniform composition of Al cannot result from strain, as the films are practically strain free (see Fig. 6.10). The most likely explanation is that the increased In content disturbs the initial steps of the InAlGaN film growth. This can be due to increased compositional fluctuation of In [117].

6.4 MOVPE growth of InGaN/InAlGaN quantum wells

The effect of the In content of the InAlGaN barrier layer on the efficiency of InGaN/InAlGaN MQW structures was studied by growing a series of five period MQW samples with varying In composition in the barrier. The InAlGaN barriers were grown using the same growth parameters as the InAlGaN films described in section 6.3. In addition one MQW structure was grown to study the performance of low In content barriers. The barriers of this sample were grown with the TMIn flow of 2.5 μmol/min. The barrier thicknesses were approximately 20 nm in all the samples. The $In_{0.07}Ga_{0.93}N$ QW layers were grown at the temperature of 794°C with the growth time of 30 s. After the growth of each InGaN layer the QW was covered by a 2 nm thick InAlGaN capping layer at the same growth temperature in order to protect the QW from the high temperature required for barrier layer growth. Table 6.1 shows the precursor flows, growth rate and the corresponding In and Al contents of the $In_xAl_yGa_{1-x-y}N$ barriers. The In and Al contents were determined by combining the results of SIMS and HRXRD measurements.

Table 6.1. In and Al contents of the barriers in InGaN/InAlGaN MQW samples and the corresponding precursor flows during barrier growth [modified from Publ. VII].

Sample	TMIn flow *	TMAl flow *	In (x)	Al (y)	Growth rate**
-	2.5	51	0.006	0.160	0.11
A3	5.14	51	0.007	0.160	0.11
-	10.27	51	0.011	0.155	0.10
C3	20.55	51	0.013	0.145	0.09
B3	46.23	51	0.016	0.130	0.08

*μmol/min, **nm/sec

Fig. 6.12 shows the HRXRD (0002) ω-2θ diffraction curves of the InGaN/InAlGaN MQW structures grown with various TMIn flows. The sharper peak is from the GaN buffer layer, and the broader peak on the right of the GaN peak comes from the InGaN/InAlGaN MQW stack. Several satellite peaks are visible in all the samples, indicating good periodicity and interface quality. The satellite peak intensity is weakened as the In content of the barriers is increased. This is at least partly due to a decrease of the interference in the MQW stack caused by the reduction of the Al content. The MQW peak is shifted towards the GaN peak as the TMIn flow during the barrier growth is increased, indicating decreased tensile strain in the MQW stack.

Fig. 6.13 shows the internal quantum efficiencies (IQEs) of the MQW samples as a function of the In content of the barrier layer. It should be noted that the barrier Al content y also changes according to Table 6.1. The IQEs were determined from the total luminescence intensity ratio of PL measured at 300 K and 15 K ($I_{300\ K}/I_{15\ K}$).

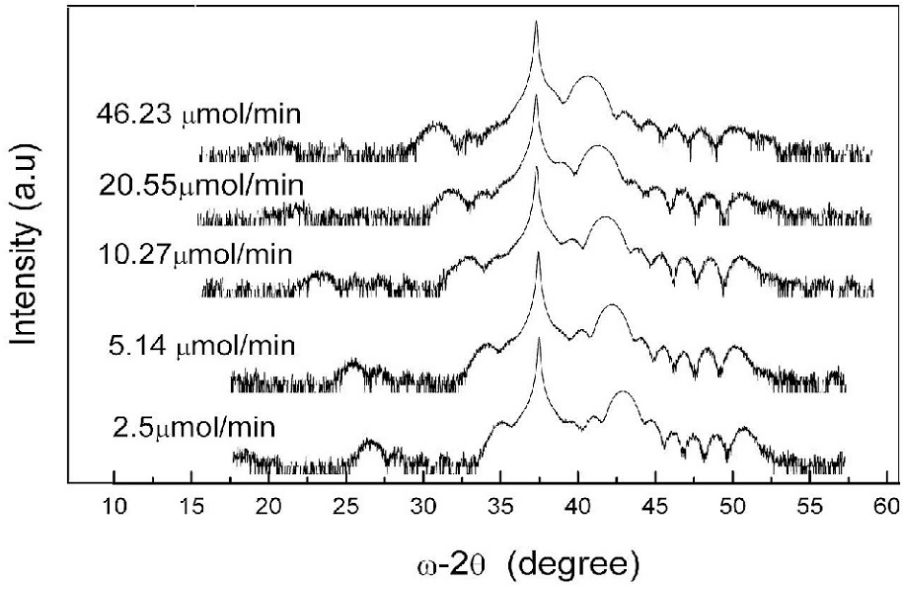

Figure 6.12. HRXRD (0002) ω-2θ diffraction curves of five period InGaN/$In_xAl_yGa_{1-x-y}N$ MQWs with different TMIn flows during growth of the $In_xAl_yGa_{1-x-y}N$ barriers [Publ. VII].

The results show that the IQE increases with increasing In content up to the In content of 0.013 and decreases rapidly at higher values. The increase of IQE is believed to result from the reduction of tensile strain in the QW stack. However, when the In content exceeds 0.013 a sharp drop in the IQE is observed. This is caused most likely by the deterioration of the material quality of the InAlGaN barriers due to increased In content. It should be noted that also the carrier confinement of the QWs is decreased as the In content of the barrier is increased. As seen in Table 6.1 the Al content is also decreased significantly and contributes a major part in the reduction of the carrier confinement. However, the reduction of the carrier confinement is unlikely to cause such a sudden drop in the IQE as observed in Fig. 6.13, because the barrier compositions of samples B3 and C3 differ only by a small amount. The inset of Fig. 6.13 shows the room temperature PL spectrum of the sample C3 with the highest IQE of 45 %. The PL peak maximum is at 383 nm and the FWHM is 18 nm.

The origin of the poor performance of the InGaN/InAlGaN MQW stack with the barrier In content of over 0.013 was examined by measuring SIMS depth profiles of the In and Al contents from the MQW structures with the barrier In content of 0.007 (sample A3) and 0.016 (sample B3). The SIMS profiles of the samples are shown in Fig. 6.14. The growth properties and barrier compositions of the samples are shown in Table 6.1. The SIMS profiles of the In composition show distinct peaks indicating the positions of the five QWs. In sample A3 the barrier Al content raises from 0.145 of the first barrier to 0.16 of the topmost barrier, and is fairly uniform

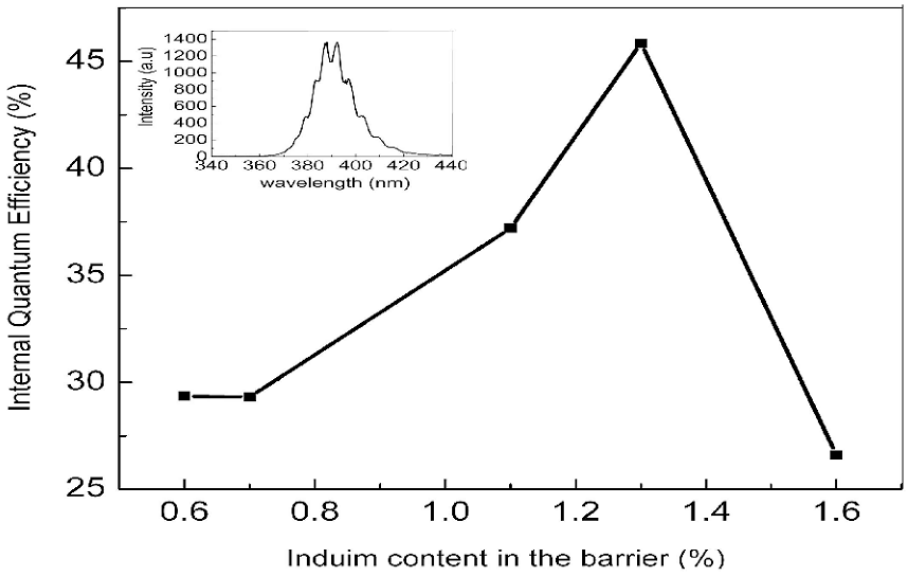

Figure 6.13. Internal quantum efficiencies of InGaN/$In_xAl_yGa_{1-x-y}N$ MQW structures as a function of barrier In content. The other MQW stack parameters are shown in Table 6.1. The inset shows the room temperature PL spectrum of sample C3 [Publ. VII].

inside of a single barrier layer. The difference of the barrier Al content is most likely caused by increased strain of the MQW. The Al content of the barriers of sample B3 is 0.13, except for the first barrier, in which the Al content increases gradually starting from the InAlGaN/GaN interface at the depth of 110 nm.

When the barrier compositions of the InGaN/InAlGaN samples are compared to the corresponding InAlGaN film compositions presented in section 6.3, we see that the InAlGaN barriers grown with the TMIn flow of 5 μmol/min (sample A3) have an identical In composition compared to the InAlGaN film grown under the same conditions (see Table 6.1 for InAlGaN barrier properties and Fig. 6.11 for InAlGaN film properties). When the TMIn flow is increased to 46 μmol/min the In content of the InAlGaN barriers (sample B3) is only 0.016 while in the InAlGaN film the In content is 0.025. The SIMS profile of sample B3 shows also peaks of Al content located on top of the QW layers indicating non-uniform barrier composition. It can be concluded that also in the case of InAlGaN barriers the increased In content disturbs the growth of the layer and results in a non-uniform composition. Also growth and the composition of InAlGaN is affected by the underlying layer, as the Al content behaves in a different way in the InAlGaN/GaN and InAlGaN/InGaN interfaces.

Fig. 6.15 shows the temperature dependence of the PL peak energy of all the InGaN/InAlGaN MQW samples. S-shape behavior is observed in the temperature dependence of all the samples. The origin of the blueshift of the s-shape lies in the

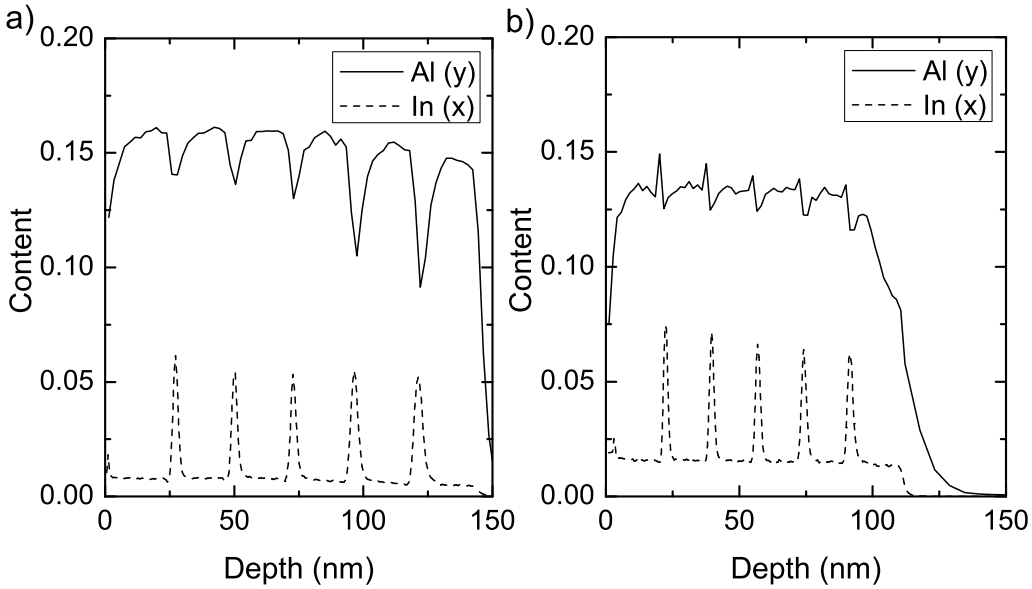

Figure 6.14. Depth profiles of the In and Al composition in the $InGaN/In_xAl_yGa_{1-x-y}N$ MQW samples A3 and B3 measured by SIMS. The MQW stack parameters are shown in Table 6.1 [Publ. IV].

localization of carriers due to potential fluctuations in the QW [118, 119]. At low temperatures the carriers are confined in the potential minima so they recombine at low energy states [119]. When the temperature is increased and the thermal energy is sufficiently high to break the localization, the emission is shifted to higher energy. Therefore, the position of the s-shape minimum is related to the depth of the localization, with the high temperature of the s-shape minimum indicating high confinement. It is seen from Fig. 6.15 that the temperature at which the s-shape minimum occurs and from where the blue shift starts is shifted to higher temperature with the increase of the barrier In content. This indicates that the increase of the barrier In content increases the localization of carriers by potential fluctuations in the QW. The potential fluctuations result most likely from composition fluctuations of the barrier layer. Larger fluctuations in the In-distribution have been reported when the In content of the InAlGaN films is increased [117]. When the In content is higher than 0.011 the confinement energy becomes larger than the thermal energy of the carriers at 300 K, so the s-shape is not observed any more. It is likely that the degradation of the InAlGaN layer quality at high In content observed earlier results from this increased fluctuation of the In composition.

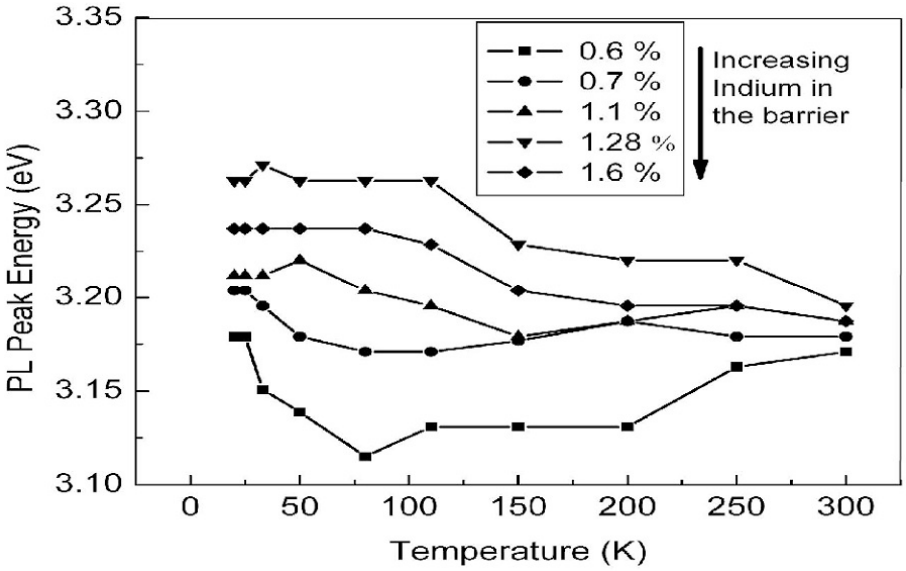

Figure 6.15. PL peak energy of the InGaN/InAlGaN MQWs with different barrier compositions as a function of temperature [Publ. VII].

6.5 Origins of high efficiency of InGaN quantum wells

Despite the high density of TDs present in InGaN MQWs the light emission efficiency of such structures is high. The origin of this defect-insensitive emission has been under a considerable study by numerous research groups. The recombination mechanism in InGaN QWs has been assigned to excitons localized at the potential minima of the QWs [120]. The potential minima are believed to originate from compositional fluctuation of the InGaN QWs [120–122]. Also well-width fluctuations have been reported to cause exciton localization in InGaN QWs [123]. The defect-insensitive properties are believed to be caused because the range of capture into a localized exciton exceeds the trapping range of non-radiative recombination centers.

Also In-rich regions or pure InN quantum dots in the InGaN QWs are assumed to play a positive role in radiative recombination, since they can act as localization centers for the carriers [121, 124]. This localization effect would prevent electrons and holes from being trapped into threading dislocations. Quantum dot like features have been observed in TEM images of InGaN QWs [125, 126]. However, high-energy electron beam damage during a TEM measurement has been observed to cause quantum dot formation [127], so the existence of quantum dots in InGaN QWs is questionable.

The effect of TDs on the performance of InGaN/GaN MQWs and LEDs was discussed in section 6.2. It was observed that the TD density did not greatly

affect the efficiency of InGaN/GaN MQWs or LEDs. A tenfold increase in the TD density only reduced the EL output of the blue LEDs at high current densities. The increase in the TD density did not affect the performance of the blue LEDs at low current densities or the performance of the green LEDs at all. It was also shown in section 6.1 that improvements in surface morphology of InGaN/GaN MQWs did not affect the overall luminous efficiency of the structures. The insensitivity of InGaN QW efficiency both on TDs and on the surface morphology can be explained by a self-screening mechanism of dislocations present in InGaN/GaN QWs [11].

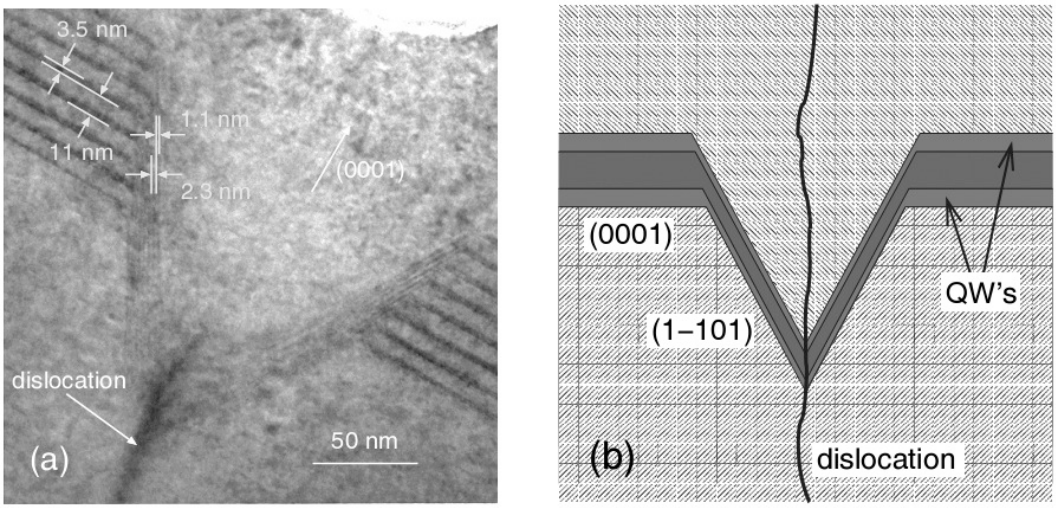

Figure 6.16. TEM image a) of an InGaN/GaN MQW structure and b) a schematic illustration of the QW structure in the vicinity of a TD induced V-pit [11].

During growth of InGaN/GaN heterostructures V-pits are formed at the TD cores as described in section 6.2. This disturbs the growth of adjacent QWs and barriers, as the V-pit size increases with increasing MQW stack thickness (see Figs. 6.1 and 6.16). It can be seen from Fig. 6.16 that the QWs and barriers grown on $(1\bar{1}01)$ sidewalls inside the V-pit have a much smaller thickness than the QWs and barriers growing on the c-plane. The smaller QW thickness causes an increased quantization and a decreased QCSE that both increase the recombination energy in the sidewall QWs [11]. Therefore, the sidewall QWs practically create a potential barrier around the TD core that screens the dislocation from carriers.

When the presence of this potential barrier is taken into account it is no surprise that the improvement of the InGaN/GaN MQW surface morphology did not cause any enhancement in the MQW efficiency as described in section 6.1. The inclusions located in the V-pits are also surrounded by the potential barrier and have little effect on the recombination efficiency of the QWs at a low excitation power. The same can be said about the InGaN/GaN MQWs and LED structures presented in section 6.2. At low operating current of LEDs the TDs are screened, regardless of the TD density.

However, when the current density is increased also the probability of the carriers reaching the dislocations increases. Therefore, a non-linear slope and different behavior of low and high TD density structures is observed in the EL intensity vs. operating current characteristics of the blue LEDs (see Fig. 6.8). However, no saturation is seen in the EL intensity vs. operating current characteristics of the green LEDs with either high or low dislocation density. This indicates that the potential barrier height is correlated with the In content of the QWs. In this case, the potential barrier height should be the smallest in UV emitting structures, as only a small In content is needed in the QWs. It has been reported that an increase in the V-pit density decreases the output power of UV InGaN LEDs [128].

Although the defect-insensitive emission and high efficiency of InGaN QWs observed in this work can be explained with the self-screening mechanism of dislocations presented above, it is by no means an established model for emission from InGaN QWs. It has also been suggested that formation of potential barriers around the dislocation cores is not an universal phenomenon, but would depend on growth conditions [10]. Also the InGaN QWs on V-defect sidewalls have been reported to have a lower band gap energy than that of the QW on the c-plane [103]. This strongly contradicts the basic assumptions of the self-screening mechanism.

Several properties of the InGaN QWs can be explained by localized excitons, such as the s-shape curve of the EL peak energy dependence on temperature (see Fig. 6.15) [118], the Stokes shift present in InGaN QWs [120], and the blue-shift of the EL peak with increasing current density [120]. However, it was shown in section 6.1 that the H_2 induced removal of In-rich clusters and surface inclusions caused no decrease in the PL intensity. Also, if In rich clusters are located at the ends of TDs [106], the assumption about the role of clusters as centers of radiative recombination is questionable. This gives strong evidence against the assumed role of In-rich emission centers acting as recombination centers.

7 Summary

In this thesis fabrication and properties of InGaN QWs was studied. The purpose was to gain insight into the emission mechanisms in the InGaN QWs and to fabricate efficient MWQ structures for near-UV, blue and green LEDs. For this purpose several InGaN/GaN and InGaN/InAlGaN MQW samples and near-UV, blue, and green LED structures were grown by MOVPE on GaN/sapphire substrates. Also growth of low dislocation density GaN buffers on sapphire by the multistep growth method (MQW) was investigated. By using the MGM it was possible to grown GaN layers with a TD density of 5.0×10^7 cm^{-2}. Compared to conventional two-step growth method the TD density of GaN layers was reduced by an order of a magnitude.

Several MOVPE process parameters were evaluated to improve the surface morphology of the InGaN/GaN MQW stack. Smooth morphology could not be achieved without deteriorating the optical quality of the QWs by increasing the growth temperature of the barriers or by annealing the barrier layers in a N_2 atmosphere. Smooth morphology, high optical quality and improved structural quality were achieved by growing the GaN barrier layers at an elevated temperature and by introducing a small amount of H_2 to the carrier gas during the barrier growth. This growth technique could not be employed in LEDs due to increased strain that caused the relaxation of the LED structure during growth. Also the efficiency of blue emitting MQW structures was found to be nearly immune to the surface morphology. However, the improved surface morphology and structural quality of the MQW stack may increase the lifetime of LEDs and laser diodes, and could be used in other applications that are sensitive to the morphology of the active region.

The properties of InGaN QWs were studied by fabricating a series of MQW and near-UV, blue, and green LED structures on GaN buffers grown by the two-step and multistep growth methods. The V-pit density on the MQW surface was found to correlate with the TD density of the GaN buffer layer. The TD density had only a minor effect on the efficiency of the InGaN/GaN MQWs or LEDs. A tenfold increase in the TD density did not affect the optical performance of blue MQW structures at low excitation and only reduced the EL output of the blue LEDs at high current densities. No effect on the performance of the blue LEDs at low current densities or the performance of the green LEDs was observed.

Poor performance of an InGaN/GaN MQW structure emitting at near-UV was attributed to the reduced carrier confinement in the QWs. Better confinement could be achieved with InAlGaN barriers. The InAlGaN layer quality was found to degrade when In content was increased over 0.025. The internal quantum efficiency of the InGaN/InAlGaN QWs was found to be sensitive to the InAlGaN barrier layer composition and to the strain state of the structure. A MQW structure emitting at 383 nm with an IQE of 45 % was presented.

The origin of the high efficiency and the insensitive nature of the InGaN QWs to the TD density could be explained by a self-screening mechanism of the TDs. Self-screening of TDs is caused by a potential barrier that is formed around the dislocation core. This could be used to describe the small effect of the improved surface morphology and TD density on the InGaN/GaN MQW structure efficiency. Also the non-linear EL intensity vs. operating current characteristics of the InGaN/GaN LEDs could be explained by the self-screening mechanism of the TDs. The height of the potential barrier was found to be dependent on the In content of the QW, and thus the effect of the TD density varied with the QW In content.

Further research in the area of this thesis should include a study of the effect of TDs on the performance and MOVPE growth of InGaN/InAlGaN MQW structures. As growth of the InGaN QWs and GaN barriers is disturbed in the vicinity of the TDs, also growth of InAlGaN barriers is certainly affected. The effect of the TDs on the composition fluctuation of the InAlGaN barriers is unknown and certainly influences the performance of the InGaN/InAlGaN MQW structures. Further study is also needed to gain insight into the strain relief mechanisms of the surface inclusions present in InGaN/GaN QWs. Also techniques for stack strain control of the MQW stack should be evaluated to enable the use of InGaN/GaN QWs free of surface inclusions in light emitting devices.

References

[1] S. Nakamura and G. Fasol, *The Blue Laser Diode* (Springer Verlag, 1997).

[2] S. J. Pearton, J. C. Zolper, R. J. Shul and F. Ren, J. Appl. Phys **86**, 1 (1999).

[3] C. Klingshirn, phys. stat. sol. (b) **244**, 3027 (2007).

[4] H. Amano, N. Sawaki, I. Akasaki and Y. Toyoda, Appl. Phys. Lett. **48**, 353 (1986).

[5] S. Nakamura, T. Mukai, M. Senoh and N. Iwasa, Jpn. J. Appl. Phys. **31**, L139 (1992).

[6] S. Nakamura, T. Mukai and M. Senoh, Appl. Phys. Lett. **64**, 1687 (1994).

[7] S. Nakamura, M. Senoh, N. Iwasa, S. Nagahama, T. Yamada and T. Mukai, Jpn. J. Appl. Phys. **34**, L1332 (1995).

[8] H. Hirayama, J. Appl. Phys. **97**, 091101 (2005).

[9] M. E. Aumer, S. F. LeBoeuf, F. G. McIntosh and S. M. Bedair, Appl. Phys. Lett. **75**, 3315 (1999).

[10] S. F. Chichibu, A. Uedono, T. Onuma, B. A. Haskell, A. Chakraborty, T. Koyama, P. T. Fini, S. Keller, S. P. DenBaars, J. S. Speck, U. K. Mishra, S. Nakamura, S. Yamaguchi, S. Kamiyama, H. Amano, A. Akasaki, J. Han and T. Sota, Nature Materials **5**, 810 (2006).

[11] A. Hangleiter, F. Hitzel, C. Netzel, D. Fuhrmann, U. Rossow, G. Ade and P. Hinze, Phys. Rev. Lett. **95**, 127402 (2005).

[12] J. Neugebauer, phys. stat. sol. (b) **227**, 93 (2001).

[13] A. R. Smith, R. M. Feenstra, D. W. Greve, M.-S. Shin, M. Skowronski, J. Neugebauer and J. E. Northrup, Surf. Sci. **423**, 70 (1999).

[14] M. Stutzmann, O. Ambacher, M. Eickhoff, U. Karrer, A. Lima Pimenta, R. Neuberger, J. Schalwig, R. Dimitrov, P. J. Schuck and R. D. Grober, phys. stat. sol. (b) **228**, 505 (2001).

[15] F. Bernardini, V. Fiorentini and D. Vanderbilt, Phys. Rev. B **56**, R10024 (1997).

[16] G. D. Chen, M. Smith, J. Y. Lin, H. X. Jiang, S.-H. Wei, M. Asif Khan and C. J. Sun, Appl. Phys. Lett. **68**, 2784 (1996).

[17] M. E. Levinshtein, S. L. Rumyantsev and M. S. Shur, *Properties of Advanced Semiconductor Materials GaN, AlN, InN, BN, SiC, SiGe* (John Wiley Sons, Inc., 2001).

[18] T. Matsuoka, H. Okamoto, M. Nakao, H. Harima and E. Kurimoto, Appl. Phys. Lett. **81**, 1246 (2002).

[19] V. Y. Davydov, A. A. Klochikin, V. V. Emtsev, S. V. Ivanov, V. V. Vekshin, F. Bechstedt, J. Furthmüller, H. Harima, A. V. Mudryi, A. Hashimoto, A. Yamamoto, J. Aderhold, J. Graul and E. E. Haller, phys. stat. sol. b **230**, R4 (2002).

[20] J. Wu, W. Walukiewicz, K. M. Yu, J. W. Ager III, E. E. Haller, H. Lu, W. J. Schaff, Y. Saito and Y. Nanishi, Appl. Phys. Lett. **80**, 3967 (2002).

[21] S. Keller and S. P. DenBaars, J. Cryst. Growth **248**, 479 (2003).

[22] M. Androulidaki, N. T. Pelekanos, K. Tsagaraki, E. Dimakis, E. Iliopoulos, A. Adikimenakis, E. Bellet-Amalric, D. Jalabert and A. Georgakilas, phys. stat. sol. (c) **3**, 1866 (2006).

[23] F. Yun, M. A. Reshchikov, L. He, T. King, H. Morkoç, S. W. Novak and L. Wei, J. Appl. Phys. **92**, 4837 (2002).

[24] S. R. Lee, A. F. Wright, M. H. Crawford, G. A. Petersen, J. Han and R. N. Biefeld, Appl. Phys. Lett. **74**, 3344 (1999).

[25] I. Vurgaftman, J. R. Meyer and L. R. Ram-Mohan, J. Appl. Phys. **89**, 5815 (2001).

[26] J. Wu, W. Walukiewicz, K. M. Yu, J. W. Ager III, E. E. Haller, H. Lu and W. J. Schaff, Appl. Phys. Lett. **80**, 4741 (2002).

[27] M. D. McCluskey, C. G. VandeWalle, C. P. Master, L. T. Romano and N. M. Johnson, Appl. Phys. Lett. **72**, 2725 (1998).

[28] J. Wu, W. Walukiewicz, K. M. Yu, J. W. Ager III, S. X. Li, E. E. Haller, H. Lu and W. J. Schaff, Solid State Commun. **127**, 411 (2003).

[29] S.-H. Wei and A. Zunger, Appl. Phys. Lett. **69**, 2719 (1996).

[30] C. Weisbuch and B. Vinter, *Quantum Semiconductor Structures, Fundamentals and Applications* (Academic Press Inc., 1991).

[31] A. Hangleiter, F. Hitzel, S. Lahmann and U. Rossow, Appl. Phys. Lett. **83**, 1169 (2003).

[32] T. Takeuchi, S. Sota, M. Katsuragawa, M. Komori, H. Takeuchi, H. Amano and I. Akasaki, Jpn. J. Appl. Phys. **36**, L382 (1997).

[33] S. F. Chichibu, A. C. Abare, M. P. Mack, M. S. Minsky, T. Deguchi, D. Cohen, P. Kozodoy, S. B. Fleicher, S. Keller, J. S. Speck, J. E. Bowers, E. Hu, U. K. Mishra, L. A. Coldren, S. P. DenBaars, K. Wada, T. Sota and S. Nakamura, Mater. Eng. Sci. B **59**, 298 (1999).

[34] H. M. Manasevit and W. I. Simpson, J. Electrochem. Soc. **116**, 1725 (1969).

[35] S. Nakamura, Jpn. J. Appl. Phys. **30**, 1348 (1991).

[36] *Thomas Swan Scientific Equipment Ltd.* (2004).

[37] M. A. Herman, W. Richter and H. Sitter, *Epitaxy, Physical Principles and Technical Implementation* (Springer-Verlag, 2004).

[38] H. E. Bennett and J. O. Porteus, J. Opt. Soc. Am. **51**, 123 (1961).

[39] R. Chierchia, T. Böttcher, H. Heinke, S. Einfeldt, S. Figge and D. Hommel, J. Appl. Phys. **93**, 8918 (2003).

[40] X. Xu, R. P. Vaudo, J. Flynn and G. R. Brandes, J. Elect. Mat. **31**, 402 (2002).

[41] D. A. Stocker, E. F. Schubert and J. M. Redwing, Appl. Phys. Lett. **73**, 2654 (1998).

[42] A. Koukitu, N. Takahashi and H. Seki, Jpn. J. Appl. Phys. **36**, L1136 (1997).

[43] A. Koukitu, T. Taki, N. Takahashi and H. Seki, J. Cryst. Growth **197**, 99 (1999).

[44] V. S. Ban, J. Electrochem. Soc. **119**, 761 (1972).

[45] T. O. Sedwick and J. E. Smith Jr., J. Electrochem. Soc. **123**, 254 (1976).

[46] S. S. Liu and D. A. Stevenson, J. Electrochem. Soc. **125**, 1161 (1978).

[47] S. C. Jain, M. Willander, J. Narayan and R. Van Overstraeten, J. Appl. Phys. **87**, 965 (2000).

[48] A. Strittmatter, A. Krost, M. Straß burg, V. Türck, D. Bimberg, J. Bläsing and J. Christen, Appl. Phys. Lett. **74**, 1242 (1999).

[49] T. W. Weeks, M. D. Bremser, K. S. Ailey, E. Carlson, W. G. Perry and R. F. Davis, Appl. Phys. Lett. **67**, 401 (1995).

[50] M. Araki, N. Mochimizo, K. Hoshino and K. Tadatomo, Jpn. J. Appl. Phys **46**, 555 (2007).

[51] T. Lang, Ph.D. thesis, Helsinki University of Technology (2007).

[52] H. P. Maruska and J. J. Tietjen, Appl. Phys. Lett. **15**, 327 (1969).

[53] K. Uchida, A. Watanabe, F. Yano, M. Kouguchi, T. Tanaka and S. Minagawa, Appl. Phys. Lett. **79**, 3487 (1996).

[54] D. D. Koleske, M. E. Coltrin, A. A. Allerman, K. C. Cross and C. C. Mitchell, Appl. Phys. Lett. **82**, 1170 (2003).

[55] M. Lada, A. G. Cullis and P. J. Parbrook, J. Cryst. Growth **258**, 89 (2003).

[56] X. H. Wu, P. Fini, E. J. Tarsa, B. Heying, S. Keller, U. K. Mishra, S. P. DenBaars and J. S. Speck, J. Cryst. Growth **189-190**, 231 (1998).

[57] X. H. Wu, L. M. Brown, D. Kapolnek, S. Keller, B. Keller, S. P. DenBaars and J. S. Speck, J. Appl. Phys. **80**, 3228 (1996).

[58] S. J. Rosner, E. C. Carr, M. J. Ludowise, G. Girolami and H. I. Erikson, Appl. Phys. Lett. **70**, 420 (1997).

[59] S. Nakamura, M. Senoh, S. Nagahama, N. Iwasa, T. Yamada, T. Matsushita, Y. Sugimoto and H. Kiyoku, Jpn. J. Appl. Phys. **36**, L1059 (1997).

[60] O.-H. Nam, M. D. Bremser, T. S. Zheleva and R. F. Davis, Appl. Phys. Lett. **71**, 2638 (1997).

[61] S. Haffouz, H. Lahrèche, P. Vennéguès, P. de Mierry, B. Beaumont, F. Omnès and P. Gibart, Appl. Phys. Lett. **73**, 1278 (1999).

[62] T. Lang, M. Odnoblyudov, V. Bougrov and M. Sopanen, J. Cryst. Growth **277**, 64 (2005).

[63] T. Hashimoto, M. Yuri, M. Ishida, Y. Terakoshi, O. Imafuji, T. Sugino and K. Itoh, Jpn. J. Appl. Phys. **38**, 6605 (1999).

[64] D. Koleske, A. E. Wickenden, R. L. Henry, J. Culbertson and M. E. Twigg, J. Cryst. Growth **223**, 466 (2001).

[65] Q. Guo and O. Kato, J. Appl. Phys. **73**, 7969 (1993).

[66] T. G. Mihopoulos, V. Gupta and K. F. Jensen, J. Cryst. Growth **195**, 733 (1998).

[67] S. Keller, G. Parish, P. T. Fini, S. Heikman, C.-H. Chen, N. Zhang, S. P. DenBaars, U. K. Mishra and Y.-F. Wu, J. Appl. Phys. **86**, 5850 (1999).

[68] M. Imura, K. Nakano, T. Kitano, N. Fujimoto, N. Okada, K. Balakrishnan, M. Iwaya, S. Kamiyama, H. Amano, I. Akasaki, K. Shimono, T. Noro, T. Takagi and A. Bandoh, phys. stat. sol. (a) **203**, 1626 (2006).

[69] M. Mesrine, N. Grandjean and J. Massies, Appl. Phys. Lett. **72**, 350 (1998).

[70] S. Keller, B. P. Keller, D. Kapolnek, A. C. Abare, H. Masui, L. A. Coldren, U. K. Mishra and S. P. DenBaars, Appl. Phys. Lett. **68**, 3147 (1996).

[71] S. Keller, B. P. Keller, D. Kapolnek, U. K. Mishra, S. P. DenBaars, I. K. Shmagin, R. M. Kolbas and S. Krishnankutty, J. Cryst. Growth **170**, 349 (1997).

[72] S. Yamaguchi, M. Kariya, S. Nitta, T. Takeuchi, C. Wetzel, H. Amano and I. Akasaki, J. Appl. Phys. **85**, 7682 (1999).

[73] J. Ou, W.-K. Chen, H.-C. Lin, Y.-C. Pan and M.-C. Lee, Jpn. J. Appl. Phys. **37**, L633 (1998).

[74] K. Hiramitsu, Y. Kawaguchi, M. Shimizu, N. Sawaki, T. Zheleva, R. F. Davis, H. Tsuda, W. Taki, N. Kuwano and K. Oki, MRS Internet J. Nitride Semicond. Res. **2**, 6 (1997).

[75] M. Shimizu, Y. Kawaguchi, K. Hiramatsu and N. Sawaki, Jpn. J. Appl. Phys. **36**, 3381 (1997).

[76] M. Asif Khan, J. W. Yang, G. Simin, R. Gaska, M. S. Shur, H.-C. zur Loye, S. Tamulaitis, A. Zukauskas, D. J. Smith, D. Chandrasekhar and R. Bicknell-Tassius, Appl. Phys. Lett. **76**, 1161 (2000).

[77] J. Han, J. J. Figiel, G. A. Petersen, S. M. Myers, M. H. Crawford and M. A. Banas, Jpn. J. Appl. Phys. **39**, 2372 (2000).

[78] F. G. McIntosh, K. S. Boutros, J. C. Roberts, S. M. Bedair, E. L. Piner and N. A. El-Masry, Appl. Phys. Lett. **68**, 40 (1996).

[79] H. K. Cho, K. H. Lee, S. W. Kim, K. S. Park, Y. H. Cho and J. H. Lee, J. Cryst. Growth. **267**, 67 (2004).

[80] R. Butté et al., J. Phys. D: Appl. Phys. **40**, 6328 (2007).

[81] E. F. Schubert and J. K. Kim, Science **308**, 1274 (2005).

[82] E. F. Schubert, J. K. Kim, H. Luo and J.-Q. Xi, Rep. Prog. Phys. **69**, 3069 (2006).

[83] F. K. Yam and Z. Hassan, Microelectronics Journal **36**, 129 (2005).

[84] J. K. Sheu, S. J. Chang, C. H. Kuo, Y. K. Su, L. W. Wu, Y. C. Lin, W. C. Lai, J. M. Tsai, G. C. Chi and R. K. Wu, IEEE Photon. Technol. Lett. **15**, 18 (2003).

[85] O. B. Shchekin, J. E. Epler, T. A. Trottier, T. Margalith, D. A. Steigerwald, H. M. O., P. S. Martin and M. R. Krames, Appl. Phys. Lett. **89**, 071109 (2006).

[86] T. Mukai, M. Yamada and S. Nakamura, Jpn. J. Appl. Phys. **38**, 3976 (1999).

[87] N. Narendran and Y. Gu, IEEE/OSA J. Display Technology **1**, 167 (2005).

[88] I. Akasaki, J. Cryst. Growth **300**, 2 (2007).

[89] S. Nakamura, N. Iwasa, M. Senoh and T. Mukai, Jpn. J. Appl. Phys **31**, 1258 (1992).

[90] Y. Nakagawa, M. Haraguchi, M. Fukui, S. Tanaka, A. Sakaki, K. Kususe, N. Hosokawa, T. Takehara, Y. Morioka, H. Iijima, M. Kubota, M. Abe, T. Mukai, H. Takagi and G. Shinomya, Jpn. J. Appl. Phys **43**, 23 (2004).

[91] O. Svensk, S. Suihkonen, T. Lang, H. Lipsanen, M. Sopanen, M. A. Odnoblyudov and V. E. Bougrov, J. Cryst. Growth **298**, 811 (2007).

[92] S. Grzanka, G. Franssen, G. Targowski, K. Krowicki, T. Suski, R. Czernecki, P. Perlin and M. Leszczyéski, Appl. Phys. Lett. **90**, 103507 (2007).

[93] S. Y. Han, H. S. Yang, K. H. Baik, S. J. Pearton and F. Ren, Jpn. J. Appl. Phys. **44**, 7234 (2005).

[94] J. Zhang, J. Yang, G. Simin, M. Shatalov, M. Asif Khan, M. S. Shur and R. Gaska, Appl. Phys. Lett. **77**, 2668 (2000).

[95] D. Zhu, M. J. Kappers, P. M. F. J. Costa, C. McAleese, F. D. G. Rayment, G. R. Chabrol, D. M. Graham, P. Dawson, E. J. Thrush, J. T. Mullins and C. J. Humpreys, phys. stat. sol. (a) **203**, 1819 (2006).

[96] S. Nakamura, Microelectronics J. **25**, 651 (1994).

[97] Y. S. Cho, H. Hardtdegen, N. Kaluza, R. Steins, G. Heidelberger and H. Lüth, J. Cryst. Growth **307**, 6 (2007).

[98] Y.-S. Lin, K.-J. Ma, C. Hsu, S.-W. Feng, Y.-C. Cheng, C.-C. Liao, C. C. Yang, C.-C. Chou, C.-M. Lee and J.-I. Chyi, Appl. Phys. Lett. **77**, 2988 (2000).

[99] I.-H. Kim, H.-S. Park, Y.-J. Park and T. Kim, Appl. Phys. Lett. **73**, 1634 (1998).

[100] Y. Chen, T. Takeuchi, H. Amano, I. Akasaki, N. Yamada, Y. Kaneko and S. Y. Wang, Appl. Phys. Lett. **72**, 710 (1998).

[101] Z. Liliental-Weber, Y. Chen, S. Ruvimov and J. Washburn, Phys. Rev. Lett. **79**, 2838 (1997).

[102] C. J. Sun, M. Zubair Anwar, Q. Chen, J. W. Yang, M. Asif Khan, M. S. Shur and A. D. Bykhovski, Appl. Phys. Lett. **70**, 2978 (1997).

[103] X. H. Wu, C. R. Elsass, A. Abare, M. Mack, S. Keller, P. M. Petroff, S. P. DenBaars, J. S. Speck and S. J. Rosner, Appl. Phys. Lett. **72**, 692 (1998).

[104] J. E. Northrup and J. Neugebauer, Phys. Rev. B **60**, R8473 (1999).

[105] J. Off, F. Scholz, E. Fehrenbacher, O. Gfrörer, A. Hangleiter, G. Brockt and H. Lakner, phys. stat. sol. (b) **216**, 529 (1999).

[106] S. M. Ting, J. C. Ramer, D. I. Florescu, V. N. Merai, B. E. Albert, D. S. Lee, D. Lu, D. V. Christini, L. Liu and E. A. Armour, J. Appl. Phys. **94**, 1461 (2003).

[107] F. Scholz, J. Off, E. Ferenbacher, O. Gfrörer and G. Brockt, phys. stat. sol. (a) **180**, 315 (2000).

[108] Y.-T. Moon, D.-J. Kim, K.-M. Song, C.-J. Choi, S.-H. Han, T.-Y. Seong and S.-J. Park, J. Appl. Phys. **89**, 6514 (2001).

[109] B. Van Daele, G. Van Tendeloo, K. Jacobs, I. Moerman and M. R. Leys, Appl. Phys. Lett. **85**, 4379 (2004).

[110] N. Nanhui, W. Huaibing, L. Jianping, L. Naixin, X. Yanhui, H. Jun, D. Jun and S. Guangdi, J. Cryst. Growth **286**, 209 (2006).

[111] J. K. Son, S. N. Lee, T. Sakong, H. S. Paek, O. Nam, Y. Park, J. S. Hwang, J. Y. Kim and Y. H. Cho, J. Cryst. Growth **287**, 558 (2006).

[112] S.-N. Lee, T. Sakong, W. Lee, H. Paek, M. Seon, I.-H. Lee, O. Nam and Y. Park, J. Cryst. Growth **250**, 256 (2004).

[113] E. Ozbay, Science **311**, 189 (2006).

[114] C.-Y. Chen, D.-M. Yeh, Y.-C. Lu and C. C. Yang, Appl. Phys. Lett. **89**, 203113 (2006).

[115] I. Gontijo, M. Boroditsky, E. Yablonovitch, S. Keller, U. K. Mishra and S. P. DenBaars, Phys. Rev. B **60**, 11564 (1999).

[116] M. E. Aumer, S. F. LeBoeuf, S. M. Bedair, M. Smith, J. Y. Lin and H. X. Jiang, Appl. Phys. Lett. **77**, 821 (2000).

[117] J. P. Liu, R. Q. Jin, J. C. Zhang, J. F. Wang, M. Wu, J. J. Zhu, D. G. Zhao, Y. T. Wang and H. Yang, J. Phys. D: Appl. Phys. **37**, 2060 (2004).

[118] R. Pecharromán-Gallego, R. W. Martin and I. M. Watson, J. Phys. D: Appl. Phys. **37**, 2954 (2004).

[119] K. S. Ramajah, Y. K. Su, S. J. Chang, B. Kerr, H. P. Liu and I. G. Chen, Appl. Phys. Lett. **84**, 3307 (2004).

[120] S. Chichibu, T. Azuhata, T. Sota and S. Nakamura, Appl. Phys. Lett. **69**, 4188 (1996).

[121] S. Nakamura, Science **281**, 956 (1998).

[122] K. P. O'Donel, J. F. W. Mosselmans, R. W. Martin, S. Pereira and M. E. White, J. Phys. Condens. Matter **13**, 6977 (2001).

[123] D. M. Graham, A. Soltani-Vala, P. Dawson, M. J. Godfrey, T. M. Smeeton, J. S. Barnard, M. J. Kappers, C. J. Humphreys and E. J. Thrush, J. Appl. Phys. **97**, 103508 (2005).

[124] H. Takahashi, A. Ito, T. Tanaka, A. Watanabe, H. Ota and K. Chikuma, Jpn. J. Appl. Phys, Part 2 **39**, L569 (2000).

[125] C. Kisielowski, Z. Liliental-Weber and S. Nakamura, Jpn. J. Appl. Phys. **36**, 6932 (1997).

[126] Y. Narukawa, Y. Kawakami, M. Funato, S. Fujita, S. Fujita and S. Nakamura, Appl. Phys. Lett. **70**, 981 (1997).

[127] T. M. Smeeton, M. J. Kappers, J. S. Barnard, M. E. Vickers and C. J. Humphreys, Appl. Phys. Lett. **83**, 5419 (2003).

[128] D. Morita, M. Yamamoto, K. Akaishi, K. Matoba, K. Yasutomo, Y. Kasai, N. S. Sano, Masahiko and T. Mukai, Jpn. J. Appl. Phys. **43**, 5945 (2004).

ISBN 978-951-22-9286-8
ISBN 978-951-22-9287-5 (PDF)
ISSN 1795-2239
ISSN 1795-4584 (PDF)